

Are elevated moist layers a blind spot for hyperspectral infrared sounders? - A model study

Marc Prange^{1,2}, Manfred Brath¹, and Stefan A. Buehler¹

¹Universität Hamburg, Meteorologisches Institut, Bundesstraße 55, 22525 Hamburg, Germany

²International Max Planck Research School on Earth System Modelling (IMPRS-ESM), Bundesstraße 53, 20146 Hamburg, Germany

Correspondence: Marc Prange (marc.prange@uni-hamburg.de)

Abstract. The ability of the hyperspectral satellite based passive infrared (IR) instrument IASI to resolve Elevated Moist Layers (EMLs) within the free troposphere is investigated. EMLs are strong moisture anomalies with significant impact on the radiative heating rate profile and typically coupled to freezing level detrainment from convective cells in the tropics. A previous case study by Stevens et al. (2017) indicated inherent deficiencies of passive satellite based remote sensing instruments to resolve an EML. In this work, we first put the findings of Stevens et al. (2017) into the context of other retrieval case studies of EML-like structures, showing that such structures can in principle be retrieved, but retrievability depends on the retrieval method and the exact retrieval setup. To approach a first more systematic analysis of EML retrievability, we introduce our own basic Optimal Estimation (OEM) retrieval, which for the purpose of this study is based on forward modelled (synthetic) clear-sky observations. By applying the OEM retrieval to the same EML case as Stevens et al. (2017) we find that a lack of independent temperature information can significantly deteriorate the humidity retrieval due to a strong temperature inversion at the EML top. However, we show that by employing a wider spectral range of the hyperspectral IR observation, this issue can be avoided and EMLs can generally be resolved. We introduce a new framework for the identification and characterisation of moisture anomalies, a subset of which are EMLs, to specifically quantify the retrieval's ability of capturing moisture anomalies. The new framework is applied to 1288 synthetic retrievals of tropical ocean short-range forecast model atmospheres, allowing for a direct statistical comparison of moisture anomalies between the retrieval and the reference dataset. With our basic OEM retrieval, we find that retrieved moisture anomalies are on average 17 % weaker and 15 % thicker than their true counterparts. We attribute this to the retrieval smoothing error and the fact that rather weak and narrow moisture anomalies are most frequently missed by the retrieval. Smoothing is found to also constrain the magnitude of local heating rate extremes associated with moisture anomalies, particularly for the strongest anomalies that are found in the lower to mid troposphere. In total, about 80 % of moisture anomalies in the reference dataset are found by the retrieval. Below 5 km altitude, this fraction is only on the order of 52 %. We conclude that the retrieval of lower to mid tropospheric moisture anomalies, in particular of EMLs, is possible when the anomaly is sufficiently strong and its thickness is at least on the order of about 1.5 km. This study sets the methodological basis to more comprehensively investigate EMLs based on real hyperspectral IR observations and their operational products in the future.

The vertical structure of tropospheric water vapor is an important driver for dynamical processes due to its effect on the radiative heating profile. In particular, Muller and Bony (2015) found that the spatial variability of the radiative heating profile gives rise to spatial self-aggregation of convection, which is thought to be a key factor for uncertainties in climate projections (Bony et al., 2015; Mauritsen and Stevens, 2015). A contributing phenomenon to the spatial variability in radiative heating profiles are moisture inversions in the tropical lower to mid free troposphere, so called Elevated Moist Layers (EMLs). To our best knowledge, EMLs were first identified by Haraguchi (1968) over the tropical eastern Pacific and independently by Ananthakrishnan and Kesavamurthy (1972) over India. A first systematic connection of these EMLs to the freezing level was brought to attention by Johnson et al. (1996), who formally distinguished between the commonly referred to trade wind inversion between 2 and 3 km (Cao et al., 2007) and another stable layer aloft that manifests during summer months just below the freezing level. Both, the trade wind inversion and the stable layer at the freezing level are capable of trapping moisture beneath and forming strong vertical humidity gradients. The stable layer around the freezing level has recently been brought to attention again within the framework for assessing the tropical lower tropospheric moisture budget introduced by Stevens et al. (2017).

While the general role of EMLs within their meso-scale environment has not yet been assessed conclusively, there are conceptual ideas about the emergence of EMLs and their impact on meso-scale atmospheric dynamics. Johnson et al. (1996) and Stevens et al. (2017) both hypothesise that EMLs preferably emerge in the vicinity of moist convective cells that penetrate the freezing level, where enhanced stability leads to detrainment of the saturated air. Stevens et al. (2017) further highlight the stabilising effect of glaciation above the freezing level within the initial convective cell on the environment, which further impedes nearby convection from penetrating the freezing level, leading to increased cloudiness and moisture. Studies investigating vertical modes of cloudiness in the tropics further support the idea of preferred convective detrainment near the freezing level (Zuidema, 1998; Johnson et al., 1999; Posselt et al., 2008). Following the findings of Muller and Bony (2015), EMLs may also contribute to the maintenance and aggregation of convection via the strong vertical gradient they induce in the radiative heating profile. The strong cooling at the EML top induces subsidence and horizontal mass convergence, while near the surface a mass divergence is induced. The mass divergence near the surface in the vicinity of convection may act to maintain the convection.

Stevens et al. (2017) conducted an observational case study of an EML present during the NARVAL-2 (Next Generation Remote Sensing for Validation Studies) measurement campaign. One method they deployed was a satellite retrieval analysis based on passive microwave and hyperspectral infrared (IR) observations, both of which showed poor performance in capturing the EML structure, suggesting that EMLs present a somewhat fundamental blind spot for passive satellite observations.

We start out by providing additional scientific context to the findings of Stevens et al. (2017) by briefly reviewing the results of other hyperspectral IR retrieval studies that investigated EML-like cases in Sect. 1.1. In Sect. 2, we introduce our own basic Optimal Estimation (OEM) retrieval setup that we extensively use later on to investigate a physical cause for missing the EML structure and to attempt a first quantitative and comprehensive analysis of moist layer retrievability. This study is based on

forward modelled (synthetic) observations to reduce the complexity of error sources (e.g. by collocation uncertainty, clouds, forward modelling errors) and to rather assess inherent limitations in resolving vertical moisture structures with hyperspectral IR observations. Section 3 introduces a framework for identifying and characterising moisture anomalies, which we use to specifically quantify the retrieval's ability to capture the moisture anomalies' vertical position, their thickness and their strength. In Sect. 4 we first apply our OEM retrieval to the EML scenario discussed by Stevens et al. (2017) to assess whether the strong temperature inversion at the EML top, when not properly resolved, is capable of masking the EML in the humidity retrieval. We want to note that we do not aim to reproduce the results of Stevens et al. (2017), but discuss a possible physical reason for their found EML blindspot. Then the retrieval is applied to forward simulated (synthetic) IASI observations based on an ensemble of 1288 clear-sky atmospheric profiles over the tropical ocean, which are part of the ECMWF diverse profile database introduced by Eresmaa and McNally (2014). Based on that, the absolute retrieval error and the smoothing error are quantified statistically in Sect. 5. Based on the framework introduced in Sect. 3 for identifying and characterising moisture anomalies, the retrieval's ability to capture the moisture structures of the test dataset and their footprint on the heating rate profile is assessed in Sect. 6. The results are summarized and final conclusions are drawn in Sect. 7.

1.1 Previous moist layer retrievals

Since mid-tropospheric moist layers are no uncommon phenomenon in the tropics (Johnson et al., 1996), they have shown up in hyperspectral IR retrieval case studies in the past. Although none of these studies were explicitly dedicated towards a comprehensive and quantitative analysis of retrieving EMLs, they still give a qualitative impression of the possibilities and limitations in resolving these features based on various retrieval methods and give some context to the results of Stevens et al. (2017).

A particularly performant and versatile retrieval approach was introduced by Smith et al. (2012) that is based on Empirical Orthogonal Function (EOF) regression and combines a clear-sky and cloud trained retrieval to allow for retrievals above clouds and below thin or broken clouds. The method is commonly referred to as Dual Regression (DR) retrieval. In a case study of retrieving temperature and humidity profiles in the eye of hurricane Isabel in 2003, Smith et al. (2012) demonstrate the retrieval's ability to capture the general tropospheric moisture structure in the presence of shallow cumulus clouds that go along with a vertically extended EML between 850 to 550 hPa. However, no highly resolved reference soundings are available for this case study. Weisz et al. (2013) further elaborate on the DR retrieval methodology, with particular focus on cloud top height retrieval and they present some additional case studies for clear-sky and cloudy scenes. The NCEP (National Center for Environmental Prediction) GDAS (Global Data Assimilation System) analysis product is used as a reference for the retrieved profiles and particularly large deviations are found for the clear-sky case, where a less pronounced moist layer is not resolved by the retrieval in the mid troposphere.

Latest advances in the DR retrieval with regard to vertical resolution are presented by Smith and Weisz (2018), who try to account for the effect that the regression tends to alias the retrieval towards the mean state of the test data base, suppressing vertical variability. They do so by applying their DR retrieval to forward simulated spectra of NCEP GDAS analysis, the resulting profiles of which are used to dealias the observational retrieved profiles. Smith and Weisz (2018) show in a case study

that the DR retrieval by itself is not able to resolve a significant mid tropospheric moist layer, but the dealiasing method allows to resolve its general structure. For this study a well collocated radiosonde serves as reference.

95 Another EML retrieval case study is conducted by Zhou et al. (2009), who use a slightly different retrieval scheme than the previously introduced DR method. While Zhou et al. (2009) also apply an EOF regression retrieval with clear-sky and cloudy specific regression coefficients in a first step, they additionally apply a physical OEM retrieval in a second step. The retrieval is applied to IASI observations from the Joint Airborne IASI Validation Experiment (JAIVEx), where dedicated collocations between in-situ soundings and IASI onboard MetOp-A were achieved. A particularly well collocated dropsonde profile shows
100 a strongly pronounced EML between 3 to 6 km altitude, which the IASI retrieval is able to capture well, given the expected smoothing error due to limited vertical resolution. It may well be that the additional physical retrieval step is what makes the difference in being able to retrieve an EML, when compared to the previously discussed results of the DR retrieval. This is supported by results of Calbet et al. (2006) who investigated the ability of different retrieval algorithms implemented in the EUMETSAT (European Organisation for the Exploitation of Meteorological Satellites) IASI L2 processor to resolve vertical
105 moisture and temperature structures based on AIRS (Atmospheric Infrared Sounder) data. In particular, Calbet et al. (2006) use a collocated clear-sky radiosonde that shows a mid tropospheric moist layer. While the EOF regression retrieval shows no hint of the moist layer, the iterative physical retrieval scheme is able to resolve the structure quite well.

As a final reference, Chazette et al. (2014) investigated EUMETSAT's IASI L2 product performance based on collocated ground based Raman lidar observations from two field experiments. The comparison is done for clear-sky conditions and from
110 ground up to about 6 km altitude. Some significant vertical moisture variability, including moist layers, is captured by the lidar in the mid troposphere in several cases, but appears to not at all be resolved by the IASI retrieval. In their conclusions, Chazette et al. (2014) report that the IASI L2 processor would be complemented by microwave sounder data from the MetOp instrument suite in a future version, in particular to improve vertical resolution. We can confirm that this has been implemented to the current IASI L2 processor (EUMETSAT, 2017), but we are not aware of a dedicated followup study on retrievability of the
115 vertical moisture structure.

From this discussion of mid tropospheric moist layer retrieval case studies we conclude that such atmospheric features do not generally appear to pose a blindspot for hyperspectral IR observations. While purely EOF regression based methods seem to systematically struggle to resolve non-trivial moisture structures, OEM based methods show clear capabilities of resolving them. Hence, the absence of the strongly pronounced EML investigated by Stevens et al. (2017) in their OEM retrievals
120 rather motivates a re-investigation of the exact retrieval setup that was applied rather than be interpreted as a consequence of inherent limitations in passive remote sensing observations. By applying the basic OEM retrieval scheme introduced in the next section to synthetic IASI observations of the dropsonde profiles discussed by Stevens et al. (2017) we want analyse whether temperature induced errors act as a plausible physical cause for the absence of the EML in the retrieval in Sect. 4.

2 The retrieval

125 Extracting atmospheric state variables such as the temperature or concentrations of atmospheric constituents from passive satellite observations generally poses an under-constrained inverse problem. Sophisticated methods are required to regularise the problem, some of which were already mentioned in the previous section. The OEM approach showed the most promising results for resolving non-trivial moisture structures in the studies discussed in Sect. 1.1, but was also used for the missed EML case of Stevens et al. (2017). This motivates the introduction of our own OEM retrieval setup to more systematically
130 assess possibilities and limitations in resolving EMLs. Note that we do not aim our retrieval to be particularly performant or as versatile as operational retrieval schemes (EUMETSAT, 2017; Smith and Barnet, 2020; Berndt et al., 2020). Instead, we use the retrieval as a tool to assess basic moist layer retrievability on a low level of complexity. The formalism used in this work strongly follows the comprehensive framework introduced by Rodgers (2000). Within the next subsections the technical implementation of the retrieval setup used in this study is introduced.

135 2.1 Spectral setup

The retrieval setup of this study aims at resolving the vertical structure of water vapor in the troposphere, with particular focus on EML scenarios. The rotational-vibrational water vapor absorption band centered around $6.25 \mu\text{m}$ (1594.78 cm^{-1}) (see Fig. 1) offers rich vertically distributed information. We use all IASI channels in the range between 1190 to 1400 cm^{-1} , following the work of Schneider and Hase (2011), who demonstrated the suitability of this spectral range for retrieving profiles
140 of water vapor and its secondary isotopologues.

The spectral signal of water vapor depends not only on the atmospheric water vapor itself but also on the temperature, surface emissivity and temperature, methane and nitrous oxide. Schneider and Hase (2011) and Borger et al. (2018) concurrently found that temperature induced errors can yield up to 15 % relative error for the lower to mid tropospheric H_2O retrieval, which is significant compared to other sources of error, such as interfering species. Therefore, unresolved temperature features may
145 falsely be interpreted as water vapor signals. We assume that this is particularly relevant for EML scenarios because the strong vertical humidity gradients typically go along with temperature inversions. To reduce this error, we add independent temperature information to the retrieval from the spectral range between 645 to 800 cm^{-1} , which is part of the CO_2 absorption band centred around $15 \mu\text{m}$ (666.67 cm^{-1}). The shading in Fig. 1 indicates the H_2O degrees of freedom calculated as the trace of the averaging kernel matrix when only each respective channel is used (Rodgers, 2000). It is apparent that water
150 vapor absorption is significant throughout most of the thermal IR spectrum, yielding DOF values close to unity. Blue shading indicates where water vapor independent information can be extracted from the spectrum, which is desirable to maximize temperature information content. Note that channels are highly redundant, so DOFs of individual channels do not add up. The total DOF for water vapor in the used channel set is approximately 12.9, for temperature 23.5 and for surface temperature 0.99. Interestingly, Fig. 1 visually shows that the shortwave CO_2 band is associated with less water vapor interference in its
155 flank between around 2200 to 2300 cm^{-1} than the longwave CO_2 band. However, due to known daytime dependent non-LTE

associated biases and a worse signal to noise ratio in the shortwave channels of IASI (Razavi et al., 2009; Matricardi et al., 2018; Clerbaux et al., 2009), we only use the longwave CO₂ channels.

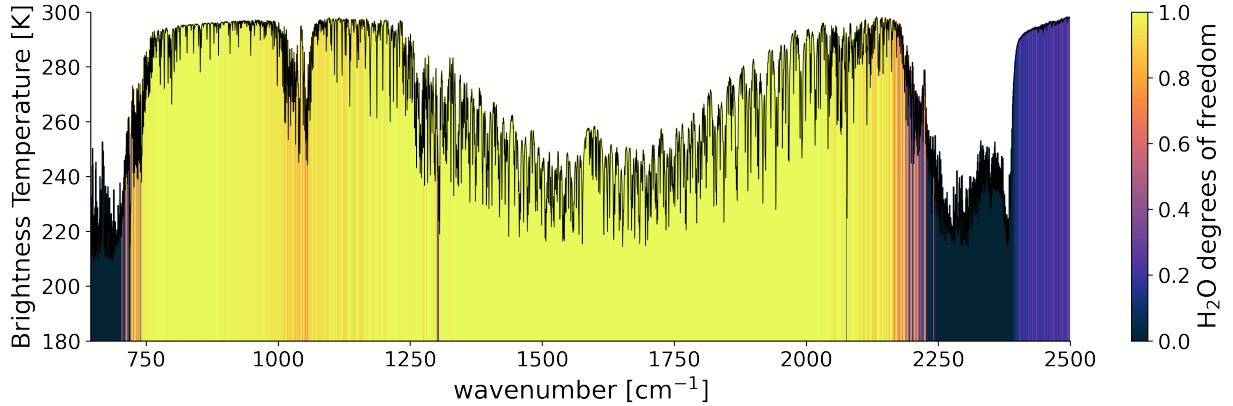


Figure 1. Forward simulated spectrum in the spectral range of the IASI instrument. Colors denote the water vapor information content of individual channels calculated as the trace of the averaging kernel matrix when only each respective channel is used. Hence, the colored shading does not account for redundancy of information between channels, but simply conveys where water vapor absorption is significant.

To assure that the radiative background of the surface is represented well in the retrieval, 5 window channels are added to the spectral setup that have been identified by Boukachaba et al. (2015) as suited window channels. The channels are located at wavenumbers 901.5 cm⁻¹, 942.5 cm⁻¹, 943.25 cm⁻¹, 962.5 cm⁻¹ and 1115.75 cm⁻¹. The complete spectral setup encompasses 1464 channels.

As a final note on the channel selection, the aim with our retrieval is not to make it computationally efficient, but to use it as a tool to explore the limitations in resolving vertical moisture features with IASI. Hence, we do not employ any channel selection method, although we are aware of the rich literature in this context (Fourrié and Thépat, 2003; Fourrié and Rabier, 2004; Collard, 2007; Martinet et al., 2013; Chang et al., 2020, among others).

2.2 Retrieval quantities

The quantities targeted for retrieval in this study are the profiles of water vapor volume mixing ratio ($\text{VMR}_{\text{H}_2\text{O}}$), temperature (T) and the surface temperature (T_s). They are represented by the retrieval state vector \mathbf{x} :

$$\mathbf{x} = \begin{pmatrix} \log(\text{VMR}_{\text{H}_2\text{O}}) \\ T \\ T_s \end{pmatrix} \quad (1)$$

The water vapor profile is retrieved in natural logarithmic units, which is favourable for two reasons. Firstly, $\text{VMR}_{\text{H}_2\text{O}}$ is a quantity that ranges over several orders of magnitude from a few percent near the surface to $O(10^{-6})$ in the upper troposphere

and above, which is numerically inconvenient for the optimisation algorithm. Secondly, the transformation to logarithmic units avoids the possibility of physically implausible negative VMR values.

175 The major interfering trace gas species in the chosen spectral region that are not part of the retrieval state vector x are CH₄ and N₂O. Based on the error budget analysis conducted by Schneider and Hase (2011) it is not expected that these species are significant sources of error compared to errors in the temperature profile. Hence, for simplicity, we include CH₄ and N₂O in the absorption setup, but use fixed profiles and do not retrieve them.

2.3 Optimal estimation algorithm

180 Besides the state vector depicted in Eq. 1, our OEM setup includes profiles of other atmospheric absorption species, namely N₂, N₂O, CH₄, O₂, CO₂ and O₃ as fixed forward model parameters. To account for nonlinearity, an iterative Levenberg-Marquardt (LM) solver (Levenberg, 1944; Marquardt, 1963) is used, which as input, besides the (synthetic) spectrum needs a priori and measurement covariance matrices, an a priori state vector and Jacobians, calculated for each iteration step by a forward model. We follow the notation introduced by Rodgers (2000), who provides an elaborate description of the procedure.

2.4 The forward model and representation of IASI

185 The radiative transfer model used in this study is version 2.5.0 of the Atmospheric Radiative Transfer Simulator (ARTS). A comprehensive and compact description of ARTS is provided by Eriksson et al. (2011) and Buehler et al. (2018) and more documentation can be found on the ARTS website (<https://www.radiativetransfer.org>). Here, only the features that are directly relevant for the conducted retrieval calculations are presented.

190 ARTS calculates the emitted radiation and its transmission through a given atmospheric state on a line-by-line basis. Spectral line data were taken from the HITRAN (High Resolution Transmission) molecular spectroscopic database (Gordon et al., 2017) and continuum absorption of water vapor, oxygen, nitrogen and CO₂ are represented by the MT_CKD model for continuum absorption (Mlawer et al., 2012).

195 The radiative transfer simulations are conducted as monochromatic pencil beams on a frequency grid with a resolution of 0.25 cm⁻¹, which coincides with the spectral sampling interval of IASI. The obtained spectra are then convolved with a Gaussian weighting function with a Full Width at Half Maximum (FWHM) of 0.5 cm⁻¹ to mimic the spectral response function of IASI. These technical specifications are taken from Coppens et al. (2019). Gaussian noise with a standard deviation of 0.1 K is added to the forward simulated spectra to represent the radiometric noise of IASI within the spectral range used in this study (Clerbaux et al., 2009). The sensor is assumed to be in 850 km altitude and to have a nadir viewing direction. The atmospheric cases simulated are limited to clear-sky and are above ocean surfaces, where the surface emissivity in the spectral
200 region covered by IASI is assumed to be 1.

The ARTS internal OEM module, which is part of ARTS as of version 2.4.0, is used to conduct the actual retrieval calculations.

2.5 A priori assumptions

The a priori assumptions about the atmospheric state are defined as the knowledge about the state prior to the measurement. Although the true state is always known within the frame of this model study, the a priori knowledge is chosen based on information that would also be available in the situation of a real measurement. The a priori knowledge is represented by an a priori state vector \mathbf{x}_a and a covariance matrix \mathbf{S}_a . For the definition of the a priori state the tropical mean atmospheric state from the profile database of Anderson et al. (1986) is used as a basis, which from now on will be referred to as tropical FASCOD (Fast Radiative Signature Code) atmosphere.

Where not stated otherwise, the a priori surface temperature is assumed to be the true surface temperature with an added Gaussian noise of 1.5 K. The Gaussian noise aims to simulate the accuracy of a real a priori surface temperature estimate, which can for example be obtained from AVHRR (Advanced Very High Resolution Radiometer), which together with IASI is part of the MetOp satellite's payload. Here, 1.5 K is a conservative assumption for tropical ocean surfaces since uncertainties in AVHRR sea surface temperature data records are typically an order of magnitude lower, e.g. estimated at 0.18 K in the dataset of Merchant et al. (2019).

The a priori temperature profile is assumed to be moist adiabatic up to around 100 hPa. The a priori surface temperature is used as a starting point for the moist adiabat. A moist adiabatic tropospheric temperature profile is a reasonable assumption because the temperature lapse rate is mostly set to be moist adiabatic within the tropics by deep convection and by the homogenisation of the temperature field by gravity waves due to the lack of a Coriolis force (Sobel and Bretherton, 2000). Around 100 hPa and above, the moist adiabat is relaxed to the tropical FASCOD atmosphere with a hyperbolic tangent weighting function to represent the tropopause and the atmosphere above. The a priori $\text{VMR}_{\text{H}_2\text{O}}$ profile is defined by combining a fixed relative humidity profile (RH) and the a priori temperature profile by using the relation:

$$\text{VMR}_{\text{H}_2\text{O}} = \frac{\text{RH} e_s(T)}{p} \quad (2)$$

The fixed tropical FASCOD RH profile is used and the equilibrium pressure of water vapor $e_s(T)$ is calculated based on the a priori temperature profile. p is the atmospheric pressure in a given altitude. $e_s(T)$ is calculated as the equilibrium pressure over water for temperatures above the triple point and over ice for temperatures more than 23 K below the triple point. For intermediate temperatures the equilibrium pressure is computed as a combination of the values over water and ice according to the IFS documentation (ECMWF, 2018).

The a priori assumption about the variability of the retrieval quantities is encoded by \mathbf{S}_a , which consists of blocks for each retrieval quantity. For the surface temperature, a variance of 100 K² is assumed. The diagonal elements of the temperature profile block of \mathbf{S}_a (Fig. 2b) are calculated based on tropical ocean profiles from the database provided by Eresmaa and McNally (2014), which is based on the ECMWF IFS forecast model with a focus on a broad sampling of temperature profiles. The nondiagonal elements are calculated based on a correlation length that linearly increases from 2.5 km at the surface to 10 km at and above the tropopause.

235 For the water vapor covariances (Fig. 2c), the approach of Schneider and Hase (2011) is adapted, where the diagonal elements of the log-scale water vapor covariances are set to 1 in the troposphere and linearly reduce to 0.25 within the stratosphere. An adjustment made here is that below 2 km, which is a crude estimate for the boundary layer height above ocean surfaces, the diagonal value linearly decreases to 0.1 at the surface. This better represents the generally fixed moisture structure near the tropical ocean surface. The nondiagonal elements are calculated based on the same correlation length approach as for the
240 temperature covariances.

An additional constraint about the atmospheric variability is introduced by filling in values for the cross-covariances between the three retrieval quantities. The diagonals of the cross covariance blocks are calculated as the product of the diagonals of the two respective covariance blocks, multiplied with a scale factor that exponentially decreases from 1 at the surface to $1/e$ in a given altitude. This altitude is chosen to be 100 m for the cross covariance between surface temperature and temperature to
245 represent the dependence of the atmospheric temperature on the surface temperature. Between temperature and water vapor the altitude is chosen to be 1000 m to represent the dependence of water vapor on temperature within the boundary layer, where the water vapor content is mainly constrained by the saturation pressure, which is mainly a function of temperature. The nondiagonal elements of the cross-covariances are calculated with the same correlation length approach as for temperature and water vapor. Figure 2(a) shows the resulting cross-covariance matrix, which only has significant values within the boundary
250 layer.

3 Definition and characterisation of moisture anomalies

This section introduces a quantitative framework to identify and characterise EMLs. This framework aims to provide an intuitive description of moisture anomaly features through a number of scalar moisture anomaly characterisation metrics and allows for a more targeted evaluation of retrieval results in Sect. 4 and 6.

255 At the core of this moisture anomaly identification method is the definition of a reference humidity profile, against which the anomalies occur. There are several ways a reference profile can be constructed and the suitability of a definition depends on the aim of the analysis. For example, a simple climatological mean profile may be a suited reference if one is interested in the mean anomaly (e.g. the bias) of a test dataset of humidity profiles. However, for the purpose of this study it is not of interest whether a humidity profile is generally rather moist or dry, but instead only anomalous vertical variability of humidity
260 is of interest. This is because the vertical moisture variability is what manifests as a footprint on the heating rate profile (Q) and thereby affect the vertical stability or even yield vertical motion (Albright et al., 2020).

To capture moisture anomalies closely related to the vertical moisture variability, the reference profile is constructed by least-square fitting a quadratic function to the $\log(\text{VMR}_{\text{H}_2\text{O}})$ profile of the troposphere up to 100 hPa. A quadratic function is preferable over a linear function because in many cases the $\text{VMR}_{\text{H}_2\text{O}}$ profile shows large scale non-exponential variability

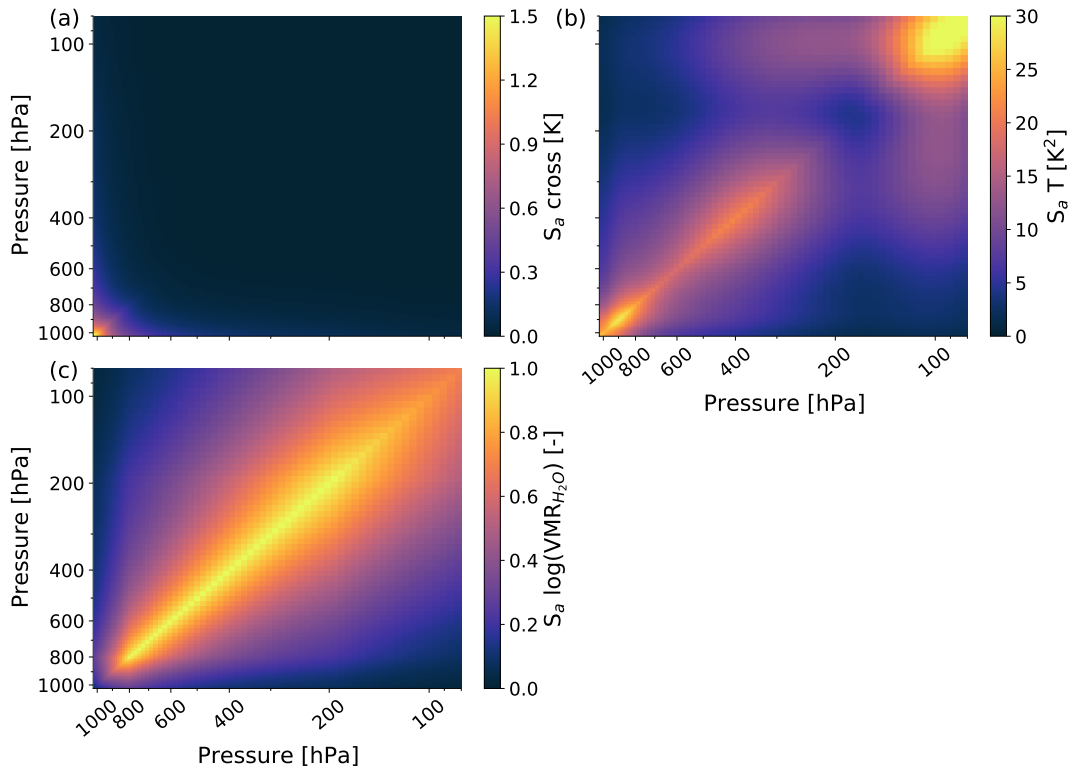


Figure 2. Covariance matrices of $\log(\text{VMR}_{\text{H}_2\text{O}})$ (c), temperature (b) and the cross-covariance matrix between water vapor and temperature (a) used for the retrieval in this study. Each of these matrices constitutes a block within the full covariance block matrix \mathbf{S}_a . Note that it is sufficient to show only one cross-covariance matrix block, since \mathbf{S}_a is block symmetric.

265 which should not interfere with the more small-scale anomalies we want to characterise. The following function is used as the reference water vapor profile:

$$\log(\text{VMR}_{\text{H}_2\text{O}, \text{ref}}) = az^2 + bz + c \quad (3)$$

The humidity at the surface is represented by $\text{VMR}_{\text{H}_2\text{O}, \text{ref}}(z = 0) = \exp(c)$ and is fixed to the surface value of the actual humidity profile. The altitude z is used as a height coordinate for fitting because compared to pressure it has the benefit that
 270 $z = 0$ at the surface. The coefficients a and b are determined by least-square fitting to the logarithm of the humidity profile between the surface and 100 hPa because the assumed relation becomes less valid closer to the tropopause. After calculating the reference profile, moisture anomalies can be identified and characterised.

To visualise the moisture anomaly identification and characterisation procedure, we show an atmospheric scenario in Fig. 3 that includes an EML as an example. The EML associated structures include a distinct moisture inversion (increase of $\text{VMR}_{\text{H}_2\text{O}}$

275 with height) with maximum humidity at around 650 hPa. Temperature inversions at the EML top and at the distinct drop of moisture at around 900 hPa are also present (not shown).

Figure 3(b) shows the close relation between the vertical humidity structure and the net heating rate Q (longwave + short-wave), which is calculated with the radiative transfer model RRTMG (Rapid Radiative Transfer Model for GCMs, Mlawer et al., 1997) through its implementation in the radiative convective equilibrium model *konrad* (Kluft and Dacie, 2020). Q is
280 calculated for all conducted retrievals throughout this study to assess whether the vertical humidity structure is captured in a way in which also Q is represented well.

The blue and orange shading associated with moist and dry anomalies depicted in Fig. 3 visualises that by definition layers of positive and negative moisture anomalies alternate in the vertical. Each such layer can be viewed as a moisture anomaly object, which we characterise by means of the scalar metrics introduced in Table 1. These metrics include the vertical bounds of the
285 moisture anomaly in terms of altitude (z_{bot} and z_{top}), the difference of which denotes the anomaly's thickness (Δz_{anom}). The anomaly height (z_{anom}) is defined as the mean over the anomaly's height interval, weighted by the anomalous humidity within the altitude bounds. Finally, the anomaly strength (s_{anom}) is defined as the mean anomalous $\text{VMR}_{\text{H}_2\text{O}}$ within the anomaly's vertical bounds. We only consider positive (moist) anomalies that are fully captured in the pressure range between 100 and 900 hPa, e.g. the positive anomalies at the very top and bottom of Fig. 3 are neglected (grey shading) to avoid tropopause and
290 boundary layer related anomalies.

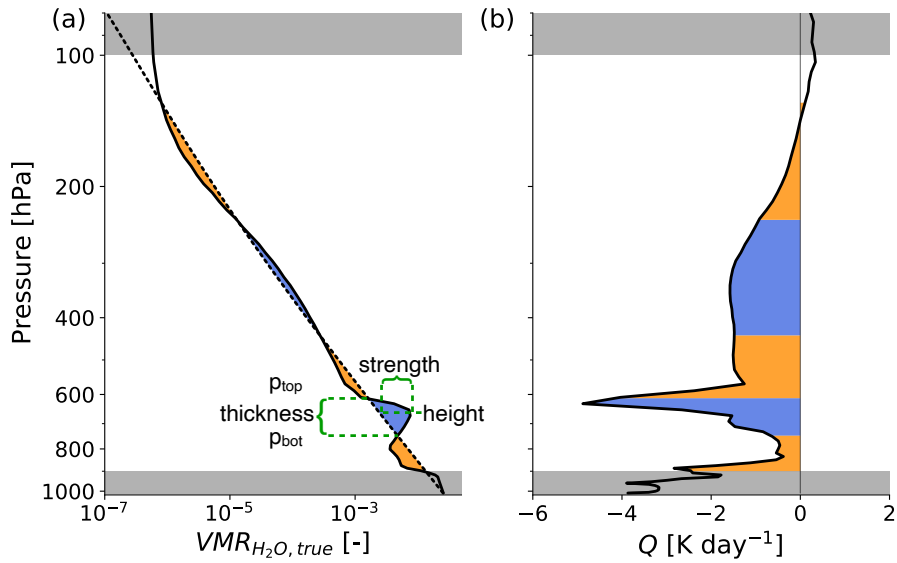


Figure 3. Humidity profile (a) of an atmospheric case with a strong EML and the associated net heating rate (longwave + shortwave) profile (b). The reference humidity profile used to identify humidity anomalies is depicted as the dashed line in (a). Layers of moist anomalies are highlighted by blue shading, dry anomalies by orange shading. Anomalies that intersect with the grey shaded regions are excluded to restrict anomalies to the free troposphere. The green lines and brackets conceptually display the definition of moisture anomaly characteristics from Table 1 for the strong positive anomaly at around 650 hPa.

Table 1. Characterisation metrics of moisture anomalies, their definitions and short descriptions. $\text{VMR}_{\text{H}_2\text{O},\text{ref}}$ denotes the reference water vapor profile.

Metric	Definition	Description
Bounds	$z_{\text{bot}}, z_{\text{top}}$	Lower and upper altitude bounds of the anomaly.
Thickness	$\Delta z_{\text{anom}} = z_{\text{top}} - z_{\text{bot}}$	Altitude interval of the anomaly.
Strength	$s_{\text{anom}} = \frac{1}{z_{\text{top}} - z_{\text{bot}}} \int_{z_{\text{bot}}}^{z_{\text{top}}} (\text{VMR}_{\text{H}_2\text{O}} - \text{VMR}_{\text{H}_2\text{O},\text{ref}}) dz$	Mean anomalous $\text{VMR}_{\text{H}_2\text{O}}$ within the anomaly.
Height	$z_{\text{anom}} = \frac{\int_{z_{\text{bot}}}^{z_{\text{top}}} z (\text{VMR}_{\text{H}_2\text{O}} - \text{VMR}_{\text{H}_2\text{O},\text{ref}}) dz}{\int_{z_{\text{bot}}}^{z_{\text{top}}} (\text{VMR}_{\text{H}_2\text{O}} - \text{VMR}_{\text{H}_2\text{O},\text{ref}}) dz}$	Weighted mean altitude of the anomaly.

4 Case study of a moist layer retrieval

In this section the retrieval introduced in Sect. 2 is applied to synthetic IASI observations of the dropsondes that sampled the EML discussed by Stevens et al. (2017). This case study is of particular interest because the found EML blindspot of Stevens et al. (2017) contradicts the results of other OEM based studies discussed in Sect. 1.1. Here we first want to specifically assess the importance of temperature information for properly resolving the moisture structure in an EML scenario. While in general it is well known that the humidity retrieval depends on the quality of the assumed or retrieved temperature profile, we argue that for EMLs this effect is of particular relevance. In a next step, the averaging kernels for the EML scenario and a mean tropical ocean atmosphere are compared to estimate the retrieval's vertical resolution and its dependence on the atmospheric state.

4.1 Importance of temperature information to retrieve a moist layer

We assess the possibility whether a lack of independent temperature information can cause the EML to not be resolved by running our retrieval in slightly altered setups. Each row of panels in Figure 4 represents a variation of the retrieval. The setup introduced in Sect. 2 is used for the first row and serves as a basis for the other two setups. We refer to this setup as retrieval setup 1. Retrieval setup 2 (Fig. 4, second row) only deviates from retrieval setup 1 by using the more narrow spectral region that was used by Lacour et al. (2012) and Stevens et al. (2017), which is limited to 1193 to 1223 and 1251 to 1253 cm^{-1} . Retrieval setup 3 (Fig. 4, third row) only deviates from retrieval setup 2 by omission of the temperature retrieval and instead setting the a priori temperature to the true reference state. The profiles that the synthetic observations are based on are denoted as "true" and the same for all retrieval setups. Based on these profiles, forward simulated synthetic IASI observations are calculated, synthetic Gaussian noise is added (see Sect. 2.5) and the retrieval is performed. As a technical note, we extrapolate

310 the dropsonde profiles (launched at about 350 hPa) into the upper troposphere and above by fitting a tropical mean atmospheric state (Anderson et al., 1986). We fit these profiles onto a 137 level vertical pressure grid of the ECMWF IFS model atmospheres that also come with an associated altitude grid (Eresmaa and McNally, 2014).

As a note on comparability of our results to Stevens et al. (2017), we want to be cautious. There are several differences in the exact way the retrieval is setup, e.g. in the assumed a priori states and covariances, the iteration scheme (Gauss-Newton vs. 315 LM) and also the radiative transfer model (Atmosphit vs. ARTS). Besides, our study is conducted in a synthetic framework, since we aim to assess the retrieval of EMLs more fundamentally than the discussed case studies did up to now. With this in mind, we tried to seek out a retrieval feature of the study of Stevens et al. (2017) that is capable of masking the EML in our setup. This feature is the used spectral region that is closely tied to the temperature information content as we want to show in the following.

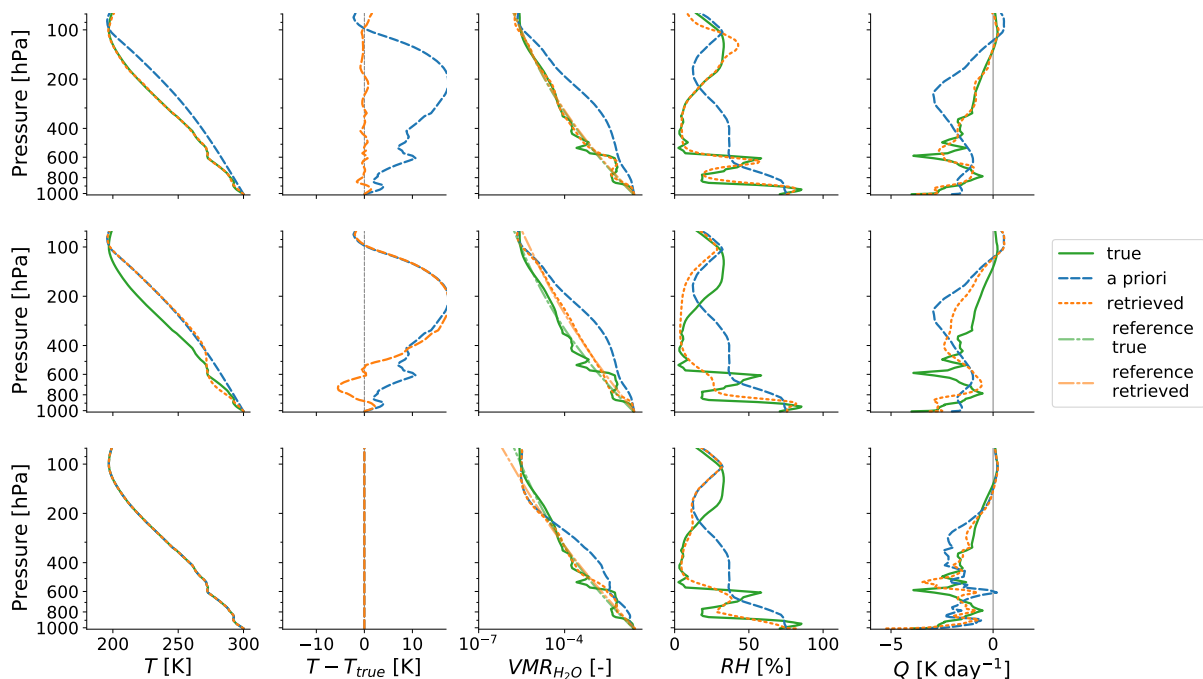


Figure 4. Columns show profiles of temperature (T), temperature differences of a priori and retrieved state to the true state, $\text{VMR}_{\text{H}_2\text{O}}$, relative humidity (RH) and net heating rates (Q) for the dropsonde profiles that sampled the EML discussed by Stevens et al. (2017) (labeled as "true" here). Displayed are the true states that are used as a basis for the forward modelled synthetic IASI observation, the a priori states of the retrieval and the retrieved states. The $\text{VMR}_{\text{H}_2\text{O}}$ reference profiles defined in Sect. 3 are also depicted. Rows show retrieval results based on different retrieval setups that are introduced in the text.

320 Looking at the retrieval results of Fig. 4, the EML structure is found to be resolved well with retrieval setup 1 while retrieval setup 2 misses the EML almost completely, comparable to the results of Stevens et al. (2017). We hypothesize that the missing EML with retrieval setup 2 is caused by the fact that with the limited spectral setup, there is no sufficient independent

Table 2. Moisture anomaly characteristics of the EML shown in Fig. 4. This table is analogous to Table 1, where the exact definitions of the different metrics are explained. The EML characteristics displayed here are calculated for the true state and the retrieval results of retrieval setup 1 and 3, corresponding to upper and lower rows of Fig. 4, respectively. Retrieval setup 2 does not feature a moisture anomaly object as defined in Sect. 3.

Metric	Variable name	True state	Retrieval setup 1	Retrieval setup 3
Bounds	$z_{\text{bot}}, z_{\text{top}}$	2.5 km, 4.8 km	3.0 km, 5.1 km	2.3 km, 6.0 km
Thickness	Δz_{anom}	2.3 km	2.1 km	3.7 km
Strength	s_{anom}	$2.8 \cdot 10^{-3}$	$2.2 \cdot 10^{-3}$	$1.1 \cdot 10^{-3}$
Height	z_{anom}	3.6 km	3.8 km	3.8 km

temperature information available for the retrieval to separate the moisture from the temperature signal, causing large retrieval errors in both quantities. While other previous retrieval studies deliberately try to account for this issue by deploying either a simultaneous retrieval approach (Smith et al., 2012; Weisz et al., 2013; Irion et al., 2018) or a sequential retrieval approach (Smith and Barnet, 2019, 2020; Susskind et al., 2014), we want to highlight the importance of doing so, specifically in an EML scenario.

We find that the large water vapor and temperature errors obtained with retrieval setup 2 around the EML altitude compensate radiatively. While the underestimated humidity at the EML altitude yields an increased spectral radiance in the used water vapor band due to a lower emission height associated with a higher emission temperature, the underestimated temperature yields a decreased spectral radiance. Since this compensation leads to comparatively low γ -costs in the OEM scheme, it explains why retrieval setup 2 finds an optimal solution that is associated with relatively large retrieval errors in both temperature and water vapor.

We introduce retrieval setup 3 to exclude the possibility that resolving the EML with retrieval setup 2 is simply limited by vertical resolution of the moisture retrieval, e.g. limited humidity information content. The retrieval results of retrieval setup 3 show that with a perfect prior temperature profile also the limited spectral range is sufficient to resolve the general EML structure, albeit with reduced EML amplitude. Hence, the EML blindspot of retrieval setup 2 and possibly of Stevens et al. (2017) is a consequence of the ambiguity that lies in the limited spectral range with respect to temperature and water vapor.

To exemplify the concept of the moisture anomaly identification and characterisation method introduced in Sect. 3 we apply the procedure to this case study and present the derived EML characteristics for each of the different retrieval setups in Table 2. To identify the EML centered around 650 hPa in the true and retrieved profiles in Figure 4 we introduce the respective reference profiles against which positive $\text{VMR}_{\text{H}_2\text{O}}$ anomalies can be identified. While retrieval setup 1 and 3 yield a moisture anomaly

that can be characterised by our method and compared to the characteristics of the true EML, retrieval setup 2 does not show a positive moisture anomaly around 650 hPa.

345 Table 2 shows that the EML in the true state is centered around 3.6 km altitude and has a vertical extent of 2.3 km. Retrieval setup 1 captures these characteristics reasonably well while retrieval setup 3 shows a strongly overestimated EML thickness of about 3.7 km, reflecting stronger smoothing caused by the limited spectral range used in this setup. Both retrieval setups show a slightly increased EML height when compared to the true state of about 200 m for reasons we can only speculate on. We could see this being a systematic effect caused a less pronounced effect of smoothing at the EML bottom due to higher optical
350 density than aloft. Since the atmosphere is optically more dense near the surface, smoothing may smear the EML over a larger altitude interval at the top than at the bottom, positively biasing the EML altitude in the retrieval.

While the EML strength s_{anom} may appear as the least trivial moisture anomaly characteristic, being without units due to its definition based on $\text{VMR}_{\text{H}_2\text{O}}$, it becomes more intuitive when values are put into relation to each other. The true EML strength of $2.8 \cdot 10^{-3}$, which reflects the mean anomalous $\text{VMR}_{\text{H}_2\text{O}}$ within the EML, is about about 30 % greater than the
355 EML strength derived from retrieval setup 1 and about 2.5 times greater than the EML strength derived from retrieval setup 3. This reflects the notion that while retrieval setup 1 is able to resolve the EML well, retrieval setup 3 yields a strongly smoothed EML that is significantly less pronounced than its true counterpart.

We conclude that while the EML investigated by Stevens et al. (2017) does not appear to pose a general blind spot for hyperspectral IR satellite observations, we are able to find a retrieval configuration that reproduces a similar result as theirs.
360 The deciding property of that configuration is the lack of independent temperature information, which in an EML scenario can yield radiatively compensating errors in temperature and water vapor. With retrieval setup 1 on the other hand, we present a retrieval setup that is able to capture both temperature and humidity profiles well, including the EML, which is in line with other OEM based moist layer case studies (Zhou et al., 2009; Calbet et al., 2006).

4.2 Retrieval resolution

365 With OEM, a more quantitative estimation of vertical retrieval resolution can easily be deduced by aid of the averaging kernel matrix \mathbf{A} (Rodgers, 2000). The rows of \mathbf{A} describe the response of the retrieved state to a perturbation in the true state, taking into account the specifications of the observing system. The averaging kernels presented here are based on the spectral setup and a priori assumptions introduced in Sect. 2.

Several previous studies showed IASI averaging kernels for mean atmospheric states (Lerner, 2002; Schneider and Hase,
370 2011; Smith and Weisz, 2018). Here we want to highlight the dependence of vertical resolution on the atmospheric state by contrasting the averaging kernels of a tropical mean atmosphere to the reference EML case discussed in the previous subsection. Smith and Barnett (2020) also considered the dependence of \mathbf{A} on the atmospheric state, which they find can be quite severe. In contrast to their more general study, we want to focus on comparing the variability of \mathbf{A} with respect to a well characterised mean and EML state. While we focus on discussing the water vapor averaging kernels in this section, similar conclusions can
375 be made about the temperature averaging kernels which are appended in Appendix A.

Figures 5(a) and (c) depict the rows of the H₂O averaging kernel matrix as colored lines for two different atmospheric setups. The more blue lines correspond to kernels closer to the surface, while the more yellow lines correspond to kernels higher up in the atmosphere. Figures 5(a) and (b) are based on an average tropical ocean atmosphere, namely the tropical FASCOD atmosphere introduced in Sect. 2.5. Figures 5(c) and (d) only differ in their base atmospheric state by the introduced EML, as described in Sect. 3. The vertical width of a kernel is a measure of the retrieval’s vertical resolution in a specific height, which is shown in terms of Full Width at Half Maximum (FWHM) of the respective kernels in Fig. 5(b) and (d). A measure for the retrieval’s ability to detect and respond to a water vapor disturbance in the true state in a given height is the measurement response, which is defined as the sum over all kernel rows and depicted as the black line in Fig. 5(a) and (c). Values close to unity indicate that the retrieval is sensitive to disturbances in the true profile (Rodgers, 2000).

The averaging kernels of the mean tropical ocean atmosphere in Fig. 5(a) expectably show a very smooth behaviour with height and the deduced vertical resolution is similar to that of Smith and Weisz (2018), e.g. it is on the order of 1.5 km throughout the free troposphere between around 200 to 800 hPa. In the upper troposphere ($p \lesssim 200$ hPa) a significant decrease in vertical resolution is found. In the boundary layer, the vertical resolution does not appear to diminish, but to improve, which is in agreement with Smith and Weisz (2018). However, we find this to be misleading because the shape of the averaging kernels associated with these altitudes is distorted due to the strong signal of the surface, not allowing for a robust calculation of the FWHM. Rather than the FWHM, the measurement response is a more informative measure of the retrieval’s sensitivity to disturbances in the boundary layer. For the tropical ocean atmosphere, the measurement response is close to unity throughout most of the free troposphere and shows a sharp decrease within the boundary layer, indicating limited sensitivity to water vapor disturbances in the true state only in the boundary layer.

The EML has a significant impact on all averaging kernels in the lower and mid troposphere as shown in Fig. 5(c) and (d). Around the humidity maximum at the EML top the averaging kernels show distinct peaks, which are caused by the strong radiative signal associated with the EML. The EML signal is so strong that it also affects the more sensitive channels that usually sample higher altitudes and therefore decreases the vertical resolution from about 1.5 km to 2.5 km between the EML top and about 200 hPa compared to the tropical mean atmosphere. As the moisture decreases beneath the EML humidity maximum, a clear reduction in vertical resolution down to about 2.5 km at around 800 hPa is found, indicating a more limited ability to resolve additional moisture features beneath the EML. This state dependence of the averaging kernel reflects the nonlinear nature of the retrieval problem and the limited expressiveness of the vertical resolution deduced with this method. Retrievability of a moisture feature not only depends on its vertical extent, but on the atmospheric state it is embedded in. This motivates the statistical analysis presented in the next section of analysing the retrieval’s performance with regard to its ability of capturing moisture anomalies as introduced in Sect. 3.

5 Retrieval performance

After the exemplified investigation of an EML case in the previous section, the retrieval performance is now assessed based on a larger test dataset. The major aim with this section is to first assess the validity of our simple retrieval setup, before using the

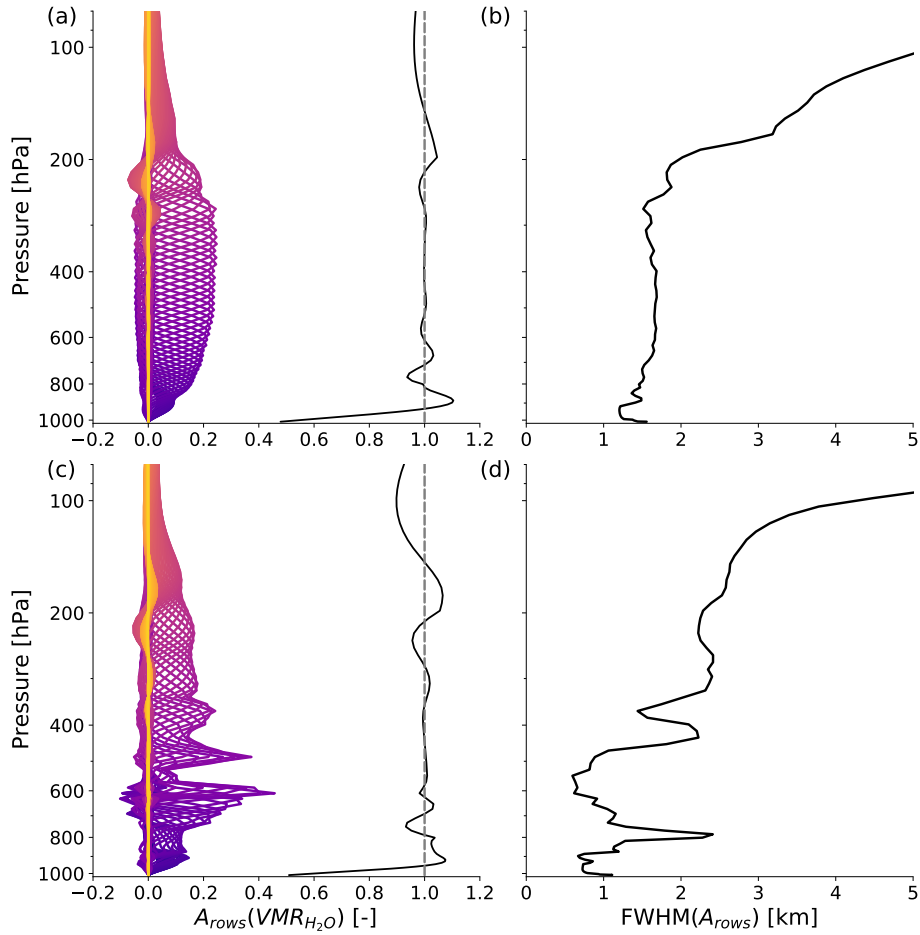


Figure 5. (a) and (c) show rows of the water vapor averaging kernel matrix ($A_{rows}(VMR_{H_2O})$) as colored lines and their sum as a black line, which denotes the measurement response. The rather blue lines correspond to kernels closer to the surface, the more yellow lines correspond to kernels in higher altitudes. (b) and (d) show the FWHM of the averaging kernel rows, which is a measure for the vertical resolution of the observing system. (a) and (b) are based on a mean tropical ocean atmosphere, specifically the tropical FASCOD atmosphere. The atmospheric setup used for (c) and (d) differs only by the introduction of EML features, as described in Sect. 3.

synthetic retrieval dataset in the next section to showcase some of the possibilities with our new method for identifying and
 410 characterising moisture anomalies introduced in Sect. 3. In the following, we first introduce the test dataset and investigate the
 vertical distribution of the retrieval error in temperature and water vapor. Afterwards, the smoothing error, which is an intrinsic
 source of error for a given observing system and a set of a priori assumptions, is calculated and discussed in the context of the
 overall retrieval error.

5.1 Reference dataset and retrieval error

415 The retrieval is applied to tropical ocean atmospheres (between 30° S to 30° N) that are part of the ECMWF IFS diverse profile
database made available by Eresmaa and McNally (2014). The database consists of 25,000 short-range forecasts, which are
divided into five even subsets that focus on representing diversity in a particular atmospheric quantity, such as temperature,
specific humidity or precipitation. For the purpose of this work, only the tropical ocean atmospheres of the subset that focuses
on a diverse sampling of specific humidity is considered. This yields a total number of 1599 atmospheric setups, for 1288 of
420 which the retrieval converges to a solution. The following analysis is based on these converged cases.

A statistical overview of the variability of temperature and humidity profiles covered by the tropical ocean dataset is pro-
vided in Fig. 6(a), (b) and (c). The temperature profiles show very limited variability, as is typical for tropical ocean regions.
However, despite this very smooth appearance of the vertical temperature structure, the individual profiles do include signif-
icant temperature inversions, for example the very prominent inversion in about 2 km height in the trade wind region (not
425 shown). The humidity profiles show weak variability within the boundary layer, where the ocean acts as a humidity source and
humidity is mostly set by the saturation vapor pressure controlled by temperature. The median RH is about 82 % at the surface
and reaches its maximum in about 500 m height in the transition to the shallow cloud layer. In the free troposphere, the typical
"C" shape structure of the RH profile is followed (Roms, 2014). An interesting feature in the 75th and 90th percentiles of
the RH profiles is the presence of positive RH anomalies in the layer between around 500 and 700 hPa, indicating moisture
430 anomalies that may be tied to the freezing level.

Figures 6(d), (e) and (f) show an overview of the retrieval's deviations from the reference dataset, from now on referred to
as the retrieval error. In the context of these figures, the term bias refers to a difference of the median values of the retrieved
and the true datasets. The temperature profile shows a positive bias close to the surface, which we attribute to the limited
signal from these heights in the satellite observation. The negative bias near the surface in RH is associated with this positive
435 temperature bias and with the slightly negative $\text{VMR}_{\text{H}_2\text{O}}$ bias near the surface. Between around 900 to 700 hPa the $\text{VMR}_{\text{H}_2\text{O}}$
and RH biases are positive, while the temperature bias is slightly negative. This positive moisture bias in the lower troposphere
is associated with an increased variability of the error, particularly towards strong positive errors that indicate an overestimation
of moisture in the lower troposphere by the retrieval. This may be caused by the typical hydrolapse that is coupled to the trade
inversion in the trade wind regions, which can in its sharpness not be captured by the retrieval.

440 In the mid troposphere between about 700 to 300 hPa, which is where typical EMLs are expected, no significant temperature
or humidity biases are found. A positive skewness in the $\text{VMR}_{\text{H}_2\text{O}}$ error distribution towards strong positive errors is found,
indicating that positive errors in retrieved $\text{VMR}_{\text{H}_2\text{O}}$ are rare, but large compared to the negative errors that occur. As an
explanation for this error pattern, we propose the idea that positive (moist) moisture anomalies tend to be captured with a slight
underestimation in their strength, while occasionally strong negative (dry) moisture anomalies beneath are associated with a
445 strong overestimation of moisture by the retrieval due to a lack of signal beneath a positive moisture anomaly (as shown in
Fig. 5). This could explain less frequent but strong positive retrieval errors and more frequent, but relatively weak negative
errors that have a net bias close to zero.

In the upper troposphere errors in temperature and humidity are generally larger. We believe that this has two causes. Firstly, the a priori moist adiabatic temperature assumption becomes worse closer to the tropopause. Secondly, Fig. 5 shows that there is only a weak radiative signal from the upper troposphere as indicated by strongly smoothed averaging kernels and a decreased vertical resolution. While this may be improved by adjusting the a priori assumptions for the upper troposphere and including even stronger absorption features of water vapor, the upper troposphere is no major concern of this study.

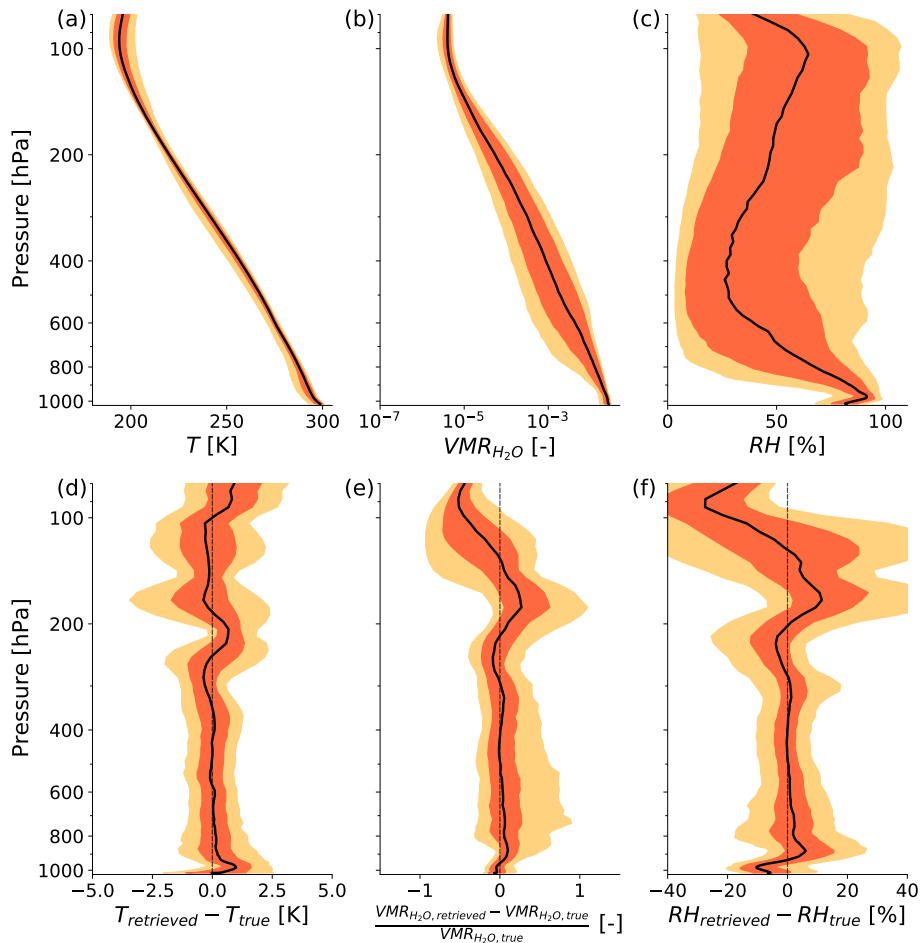


Figure 6. (a), (b) and (c) give a statistical overview of temperature, $\text{VMR}_{\text{H}_2\text{O}}$ and RH over 1288 tropical ocean model atmospheres from the dataset of Eresmaa and McNally (2014), upon which the retrieval is performed. Color scheming is based on Figure 5 of Eresmaa and McNally (2014), where bright orange indicates 10th and 90th percentiles, dark orange indicates 25th and 75th percentiles. The median is depicted by a solid black line. (e), (f), (g) show the respective statistics on the deviations of the retrieved to the true profiles. Note the exception of relative differences for $\text{VMR}_{\text{H}_2\text{O}}$, which is more suited for the dynamical range of this quantity.

5.2 Smoothing error

Part of the retrieval error shown in Fig. 6 can be attributed to the so called Smoothing Error (SE, Rodgers 2000). Given a
455 specific observing system and a priori assumptions about the quantity to be observed, the SE is a source of error that can not
be avoided without changing the observing system or a priori assumptions themselves. In the frame of the averaging kernel
matrix, the SE expresses the error in the retrieval that is associated with the non-delta-function shape of the averaging kernel
rows (see Fig. 5) and the thereby limited ability to resolve vertical features. Here, it is calculated as

$$SE = (x - x_a)(A - I_n) \quad (4)$$

460 where I_n denotes the identity matrix of order n and n is the number of vertical levels of the profile retrieval.

Figure 7 shows the SE statistics associated with the retrieved temperature and humidity profiles of the tropical ocean dataset.
The median of the SE with respect to the temperature profile ($SE(T)$) is close to zero throughout most of the free troposphere,
similar to the retrieval bias shown in Fig. 6(d). The positive retrieval bias in temperature found near the surface is with smaller
magnitude also found in $SE(T)$, indicating that this pattern is caused by a systematically unresolved vertical feature. The vari-
465 ability of the temperature retrieval error found in Fig. 6(d) in the lower and mid troposphere cannot be attributed to smoothing,
since the variability in $SE(T)$ is very small. In conclusion, this indicates that temperature error sources are unlikely to be
caused by uncaptured vertical temperature variability, but rather vertically constant errors, which do not show up in $SE(T)$.
In the upper troposphere, $SE(T)$ increases towards the tropopause where smoothing becomes the major contribution to the
retrieval temperature error.

470 For the water vapor profile in the lower and mid troposphere, smoothing is a greater source of error than for the temperature
profile (Fig. 7b). While the median of the water vapor smoothing error ($SE(\log(\text{VMR}_{\text{H}_2\text{O}}))$) is low throughout the lower and
mid troposphere, its variability (e.g. the shown percentile ranges) is on similar scale as the variability of the retrieval error
shown in Fig. 6(e). This indicates that a major contribution of error in the water vapor retrieval is to capture vertical variability.
The distribution of $SE(\log(\text{VMR}_{\text{H}_2\text{O}}))$ in the mid troposphere also reflects the positive skewness that was found in the overall
475 error in Fig. 6(e). This is consistent with the previously described idea that this skewness is linked to the retrieval's ability
of capturing vertical moisture anomalies. In the upper troposphere, the median $SE(\log(\text{VMR}_{\text{H}_2\text{O}}))$ increases to a similar
magnitude as the retrieval error, while its variability even exceeds that of the retrieval error, indicating that other sources of
error are compensating.

The $SE(\text{RH})$ statistics show the combined effect of the smoothing errors in temperature and humidity (Fig. 7c). It is apparent
480 that also in terms of RH the smoothing error has a strong contribution to the retrieval error in the lower and mid troposphere,
similar to the $\text{VMR}_{\text{H}_2\text{O}}$ error. In the upper troposphere the median $SE(\text{RH})$ is on the same order as the retrieval error, while
its variability appears to be even stronger, following the behaviour found for $SE(\log(\text{VMR}_{\text{H}_2\text{O}}))$.

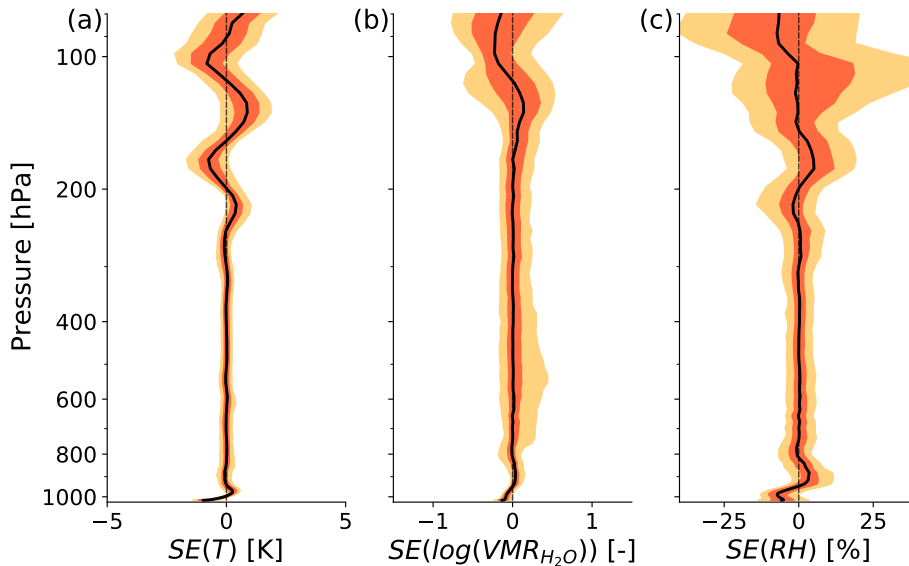


Figure 7. Smoothing Error (SE) as calculated by Eq. 4 of retrieved temperature (a), logarithmic $\text{VMR}_{\text{H}_2\text{O}}$ (b) and RH (c) profiles over 1288 tropical ocean atmospheres. Lines and shadings are defined as in Figure 6.

6 Retrieval of moisture anomalies

In this section the retrieval results for the previously introduced tropical ocean test dataset (Sect. 5) are assessed with specific
 485 focus on the characteristics of moisture anomalies as introduced in Sect. 3. First, the moisture anomaly characteristics of the tropical ocean dataset and of the retrieved dataset are compared to look for systematic limitations of the retrieval to resolve specific kinds of moisture anomalies. Then, the impact of moisture anomalies on the heating rate profile is assessed and the retrieval’s ability to capture this impact is investigated.

6.1 Moisture anomaly characteristics

490 Figure 8 shows probability density distributions of the moisture anomaly characteristics (defined in Sect. 3) for the tropical ocean dataset (green) and the associated retrieved dataset (orange). The dashed lines indicate the mean values of the respective distributions. The distributions of moisture anomaly height (z_{anom}) displayed in Fig. 8(a) show that most moisture anomalies occur in the mid to upper troposphere, which is somewhat surprising since EMLs are typically thought to be coupled to the freezing level in around 5 km height (Johnson et al., 1996; Stevens et al., 2017). However, note firstly that strong EMLs and very slight moisture anomalies are treated evenly here. Secondly, the distributions reflect the statistics of the underlying dataset,
 495 which is based on the ECMWF IFS atmospheric model. This dataset appears as a suitable starting point to assess the retrieval’s ability to capture moisture anomalies, however, the analysis of the dataset’s moisture anomaly statistics themselves are not the focus of this study.

Figure 8(a) shows a bias between true and retrieved z_{anom} of about 0.9 km, indicating that the found the z_{anom} biases in the
 500 case study of Sect. 4 do indeed appear to be systematic and even greater in amplitude. Besides the earlier proposed cause of
 a varying effect of smoothing with height, we believe this bias is also caused by a systematic underestimation of the fraction
 of moisture anomalies below 5 km altitude by the retrieval, while the fraction of anomalies above 10 km is overestimated.
 Only a fraction of about 52 % of the total number of moisture anomalies below 5 km in the reference dataset is captured by
 the retrieval. We attribute this deficiency to the fact that moisture anomalies are typically more narrow in the lower to mid
 505 troposphere than further aloft, as shown in Fig. 9.

Figure 9(a), (b) and (c) show the number of moisture anomalies of the reference dataset in the lower, mid and upper tro-
 posphere, respectively, as a function of anomaly width (Δz_{anom}) and separated into subsets of anomalies that either could
 or could not be retrieved. An anomaly of the reference dataset is considered retrieved, if there is a retrieved positive moisture
 anomaly with an anomaly height within the vertical bounds of the anomaly of the reference dataset. While it is apparent that the
 510 more narrow moisture anomalies are most frequently missed in all three altitude regions, this means a particular shortcoming
 for the retrieval between 0 to 5 km because cases with $\Delta z_{\text{anom}} \gtrsim 2$ km are especially rare. A technical cause for this is the fact
 that we exclude all anomalies that reach as close to the surface as 900 hPa (see Sect. 3). However, the lower to mid troposphere
 also is subject of more small-scale variability due to its link to the boundary layer and low level convection, making it more
 prone for small scale moisture anomalies than the free troposphere aloft.

The distribution of the moisture anomaly strength (s_{anom}) depicted in Fig. 8(b) has a similar dynamical range as $\text{VMR}_{\text{H}_2\text{O}}$
 515 since the anomalous $\text{VMR}_{\text{H}_2\text{O}}$ scales with its absolute value. The distribution of s_{anom} of the retrieved dataset is overall
 shifted towards lower values yielding a negative bias of about $-8.2 \cdot 10^{-5}$ (17 %) against the reference dataset, which can
 mostly be attributed to the smoothing error of the retrieval. The smoothing error generally acts by a weakening and thickening
 of anomalies, which also partly explains the significant positive bias of about 0.4 km (15 %) in moisture anomaly thickness
 520 (Δz_{anom}) depicted in Fig. 8(c). Another contributing effect towards the found biases in s_{anom} and Δz_{anom} is the fact that
 particularly weak and narrow moisture anomalies are more often completely missed by the retrieval as shown by Fig. 9.

6.2 Implications of moisture anomalies for the heating rate profile

Moisture anomalies affect the heating rate profile by absorbing and emitting IR radiation. Because of the exponential decrease
 of water vapor with height, emission at the anomaly top is particularly efficient and can yield a strong local radiative cooling
 525 rate (see Fig. 3). We consider this cooling effect to be the moisture anomaly's most prominent footprint on the heating rate
 profile. In the following, we quantify this cooling effect by considering the minimum heating rate within the vertical bounds of
 a moisture anomaly, $\min(Q_{\text{anom}})$. Since $\min(Q_{\text{anom}})$ is a scalar metric, it can intuitively be viewed as a function of moisture
 anomaly characteristics.

Figure 10(a) and (b) show the joint frequency distributions of the moisture anomaly strength (s_{anom}) and $\min(Q_{\text{anom}})$
 530 for the tropical ocean dataset and the retrieval dataset, respectively. Both datasets show a clear correlation between the two
 quantities, namely that stronger anomalies are associated with a stronger peak in radiative cooling. While moisture anomalies
 with $s_{\text{anom}} \lesssim 10^{-4}$ show similar minimum cooling rates down to about -2.5 K day^{-1} in both the reference and the retrieval

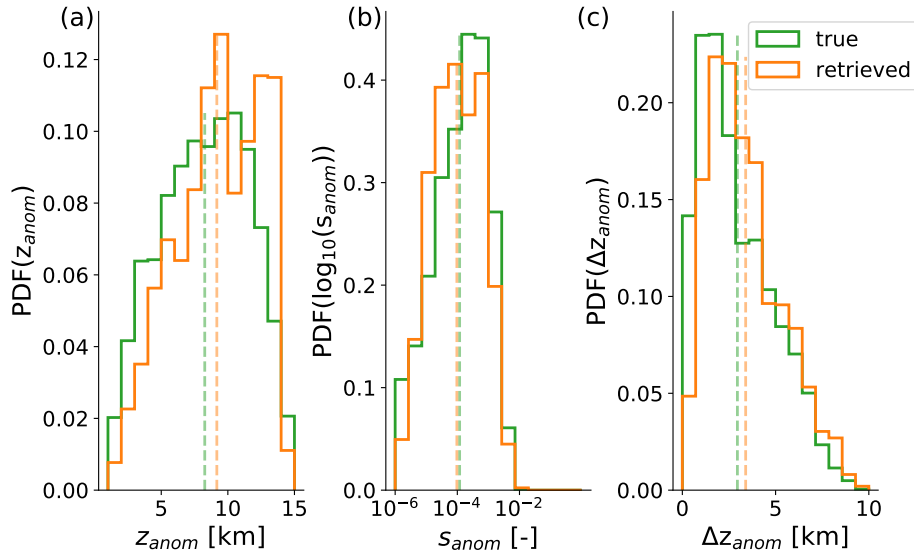


Figure 8. Probability density functions (PDFs) of moisture anomaly characteristics of the tropical ocean reference dataset (denoted as "true") and the retrieved dataset.

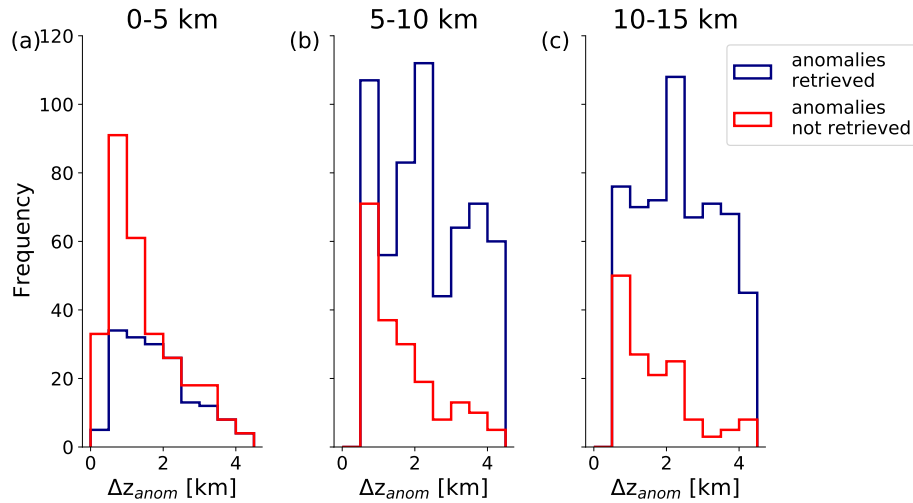


Figure 9. Frequency distributions of moisture anomaly thickness of the tropical ocean reference dataset, split up into cases where a moisture anomaly could be retrieved and could not be retrieved. (a), (b), (c) reflect three altitude regions, namely the lower (0-5 km), mid (5-10 km) and upper (10-15 km) troposphere.

dataset, larger differences between the two datasets are apparent for stronger anomalies. The reference dataset (Fig. 10, a) shows $\min(Q_{\text{anom}})$ values between about -1 to -5 K day^{-1} for moisture anomalies with $s_{\text{anom}} \gtrsim 10^{-4}$, while the retrieval dataset barely shows any $\min(Q_{\text{anom}})$ values smaller than -3 K day^{-1} .

535

We hypothesise that the increased variability in $\min(Q_{\text{anom}})$ for $s_{\text{anom}} \gtrsim 10^{-4}$ in the reference dataset can be attributed to the variability in the exact vertical shapes of the moisture anomalies. Anomalies with a strong negative moisture gradient at their top yield a stronger minimum in radiative cooling, while more smooth anomalies are associated with a less pronounced radiative cooling peak. This effect introduces more variability in $\min(Q_{\text{anom}})$ the stronger the anomalies are. It also explains
540 why retrieved moisture anomalies do not show as extreme $\min(Q_{\text{anom}})$ values as the reference dataset, since the vertical shape of retrieved anomalies is always bound by the smoothing error.

In the real world, much more extreme vertical moisture gradients associated with moisture anomalies can be observed than in the model based reference dataset used here. Albright et al. (2020) discuss an EML scenario over the Northern Atlantic Trades with a significant moisture drop that is associated with a minimum cooling rate of about 20 K day^{-1} . The results of
545 Fig. 10 indicate that while the retrieval is able to broadly distinguish between differently strong moisture anomalies and their associated heating rates, it is unable to properly represent such extreme cooling rate minima due to smoothing.

Figures 10(c) and (d) show the joint frequency distributions of the moisture anomaly strength and height (z_{anom}). A clear relation between s_{anom} and z_{anom} is found in both datasets, namely that anomalies are weaker the higher up they are in the troposphere. We explain this by the dependence of s_{anom} on the absolute humidity, which decreases exponentially with height.
550 Combining this with the relation found between anomaly strength and minimum heating rate, it is clear that the radiatively most significant moisture anomalies occur in the lower to mid troposphere. As pointed out in Sect. 6.1 when discussing Fig. 9, the retrieval has particular deficiencies in resolving the rather narrow lower to mid tropospheric moisture anomalies. It is now apparent that this deficiency is particularly relevant, since it affects the strongest and radiatively most significant moisture anomalies. However, the EML testcase investigated in Sect. 4.1 shows that when the anomaly is relatively strong and the
555 atmosphere aloft has a simple structure, also lower to mid tropospheric moisture anomalies can be retrieved well. It may be worth investigating different cases of EMLs that are embedded in a more complex tropospheric humidity structure in the future.

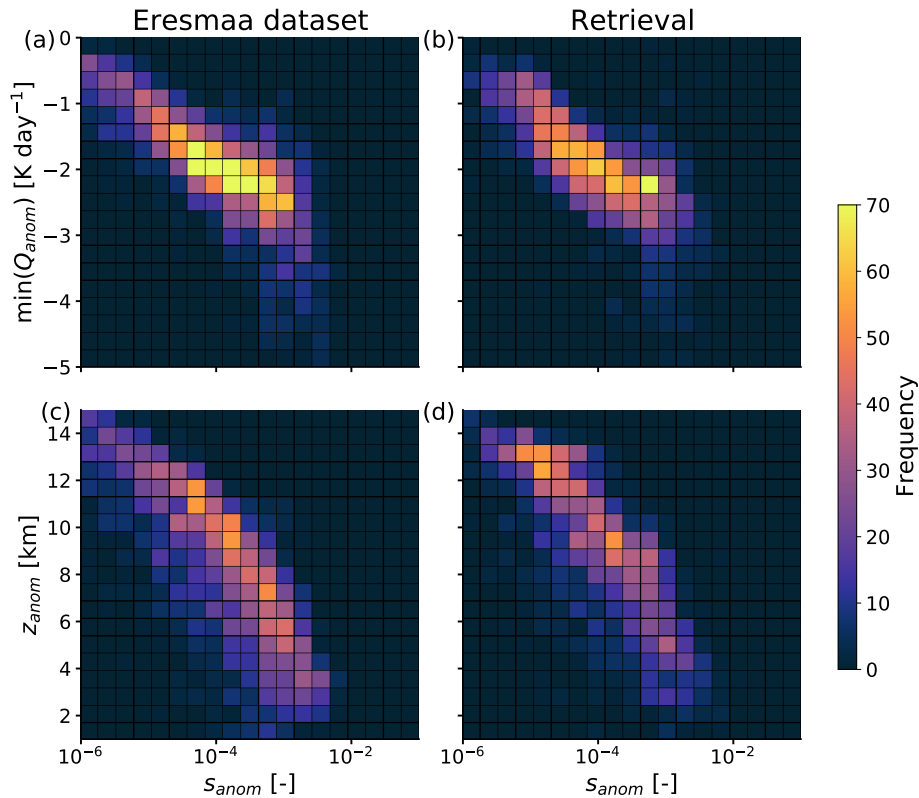


Figure 10. (a) and (b) show the joint frequency distributions of anomaly strength and minimum heating rate within the anomaly layers of the reference dataset and the retrieved dataset, respectively. (c) and (d) show the joint frequency distributions of the anomaly strength and the anomaly height for the two respective datasets.

7 Summary and conclusions

The question implicitly raised by the findings of Stevens et al. (2017), whether or not passive satellite retrievals are capable of resolving EMLs, is investigated based on a synthetic retrieval framework where the IASI instrument is represented by the forward model ARTS. An EML testcase based on dropsonde profiles from the NARVAL-2 measurement campaign (Konow et al., 2019) and a set of 1288 tropical ocean model atmospheres are used as input for the forward model and as a reference to evaluate the retrieval results against. The scenes are limited to clear sky.

To characterise an EML quantitatively (e.g. by strength, thickness and height), the concept of a moisture anomaly against a loosely fitted but clearly defined reference humidity profile is introduced. Following the ideas of Johnson et al. (1996) and Stevens et al. (2017) about a coupling of EMLs to the freezing level, EMLs would in this framework constitute a subset of rather strong, vertically confined, lower to mid tropospheric positive moisture anomalies. However, for the scope of this work no clear specification of what distinguishes an EML from other moisture anomalies is attempted, which would require a more dedicated

selection and analysis of the test dataset. Instead, the aim of this study is a first systematic evaluation EML retrievability based on hyperspectral IR observations.

570 Based on the EML case of Stevens et al. (2017), we show that with sufficient independent temperature and water vapor information, a combined retrieval of the moisture and temperature profiles and the surface temperature is capable of resolving the vertical EML structure. This result is in line with previous OEM based case studies of similar moisture structures (Calbet et al., 2006; Zhou et al., 2009). We show that limited independent temperature information can cause the EML to not be resolved by the retrieval due to compensating water vapor and temperature errors. We suggest this as a possible reason for the
575 EML blindspot found by Stevens et al. (2017).

The EML signal for the IASI instrument is further characterised by the averaging kernel and the deduced vertical resolution, which is on the order of 1.5 km for an average tropical ocean atmosphere, which is in agreement with previous studies (Lerner, 2002; Smith and Weisz, 2018). However, in the presence of an EML, the strong signal from the EML top weakens the signal from below and introduces a strong gradient in vertical resolution from 0.5 km at the EML top to 3 km at the EML bottom. This
580 state dependence of vertical resolution motivates a statistical approach to evaluate the retrieval's ability of resolving moisture anomalies in various atmospheric states.

When applying the retrieval to the tropical ocean test dataset, it is found that a large fraction of the absolute retrieval error in humidity can be attributed to smoothing. In particular in the transition region between the boundary layer and the free troposphere, the smoothing error introduces a bias to the retrieved humidity and temperature profiles, which is most likely
585 connected to the sharp humidity drop associated with the stratified barrier between the moist boundary layer and the dry free troposphere in the trade wind region. In the free troposphere, say above 800 hPa, the retrieval shows no significant moisture bias, but a positively skewed error variability, indicating that moist anomalies are typically associated with smaller errors than dry anomalies. This is coherent with the idea that dry anomalies that occur beneath moist anomalies are prone to larger errors due to the reduced sensitivity of the satellite measurement below a moist anomaly.

590 The study is completed by a specific evaluation of the moisture anomaly retrievability based on the new characterisation method introduced in Sect. 3. It is found that the retrieved moisture anomalies are on average 17 % weaker and 15 % thicker than the anomalies of the reference dataset, which we attribute to smoothing and the fact that rather weak and narrow anomalies are missed by the retrieval more often. While overall about 80 % of the total number of moisture anomalies in the reference dataset are found by the retrieval, a systematic underrepresentation of anomalies below 5 km is found, where the retrieval only
595 identifies about 52 % of the anomalies present in the reference dataset. Since it is shown that moisture anomalies in the lower to mid troposphere are typically the strongest and radiatively most significant, this issue may be quite significant.

The analysis of capturing the moisture anomalies' footprint on the heating rate profiles shows that the retrieval is able to capture the general relation between anomaly strength and minimum cooling rate. However, the retrieval shows a particular shortcoming in capturing the most extreme cooling rates associated with strong lower to mid tropospheric anomalies. We
600 attribute this shortcoming to the retrieval's limited ability of resolving strong vertical moisture gradients that are necessary for the most extreme local cooling rates. Vertical moisture gradients in the real world can be a lot stronger than the ones available

from the model test dataset (Albright et al., 2020), which means that retrieval errors with respect to peaks in the cooling rates can be large for rather extreme but realistic cases.

In summary, the retrieval result of the EML case study shows that hyperspectral IR satellite instruments are in principle
605 capable of resolving a sufficiently strong EML in an otherwise simply structured atmospheric profile. The statistical evaluation
of retrieved moisture anomaly characteristics shows that the retrieval is able to represent moisture anomalies of various thickness,
height and strength. Significant shortcomings are found in the lower to mid troposphere where about half of the moisture
anomalies are missed by the retrieval and with regard to capturing particularly strong vertical gradients, causing limitations
to resolve extreme cooling rates. It would be interesting to apply a similar analysis to operational retrieval products, such as
610 the IASI L2 product (EUMETSAT, 2017), the NUCAPS product (NOAA Unique Combined Atmospheric Processing System,
Berndt et al. 2020) or the CLIMCAPS product (Community Long-term Infrared Microwave Combined Atmospheric Product
System, Smith and Barnett 2020). The benefit of our new method for analysing moisture anomalies is that it allows for a direct
statistical evaluation of the different product's capabilities to resolve EMLs and vertical humidity structures in general by being
easy to apply to large datasets. As a next step we plan to apply our retrieval and evaluation techniques introduced in this work
615 to real hyperspectral IR observations, with focus on EML-like cases that we identify based on dropsonde observations from the
NARVAL and EUREC⁴A (Stevens et al., 2021) measurement campaigns. This may also serve as a good first testbed of data to
assess operational products' capabilities to resolve the vertical moisture structures of interest.

Code availability. The code for the radiative transfer model ARTS, which also includes the module that was used to conduct the OEM
retrieval can be found at <https://radiativetransfer.org>.

620 *Data availability.* The atmospheric profiles over tropical oceans that were used as a basis for the forward modelled IASI spectra and the
spectra themselves are publicly available on Zenodo (Prange et al., 2021). The atmospheric profiles are a subset of the ECMWF IFS diverse
profile database published by Eresmaa and McNally (2014).

Appendix A: Temperature averaging kernels

Since we highlight the importance of sufficient independent temperature information to resolve the water vapor structure, Fig.
625 A1 shows the temperature averaging kernels and deduced vertical resolution based on the retrieval setup introduced in Sect. 2.

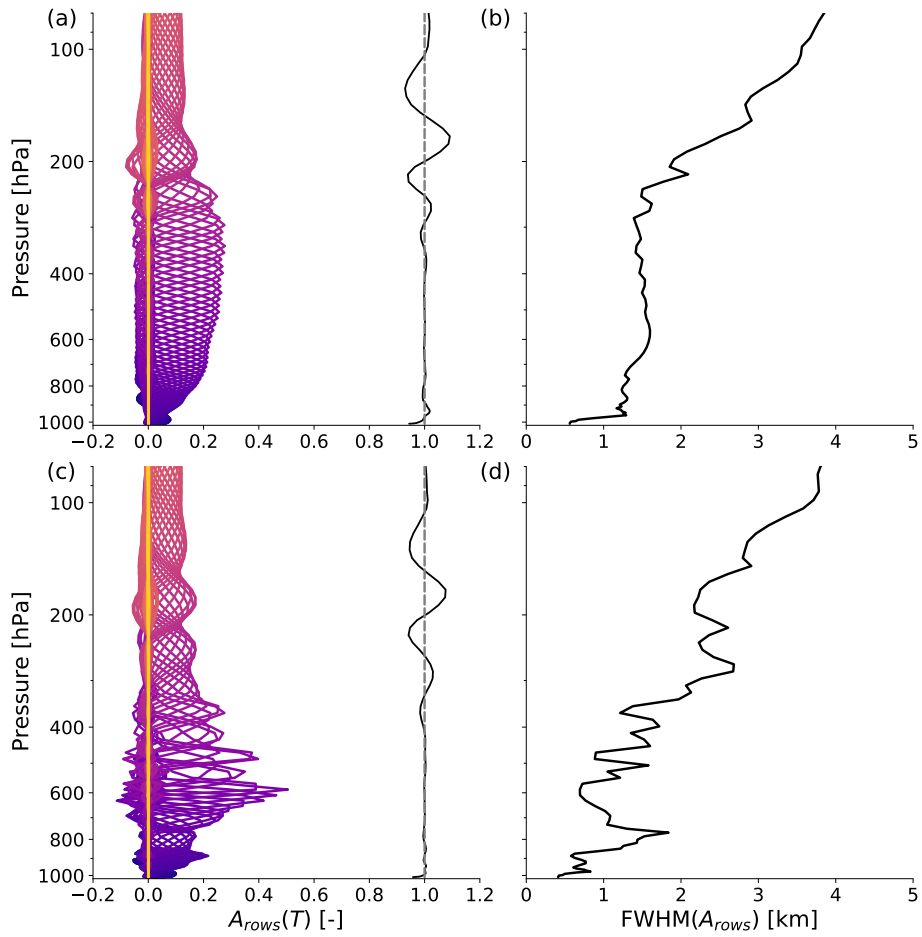


Figure A1. Same as Fig. 5, but for temperature.

Author contributions. MP conducted the radiative transfer and the retrieval calculations and prepared the manuscript. MB and SAB supervised the analysis of the retrieval results, contributed ideas to the manuscript and revised it.

Competing interests. The authors declare that they have no conflict of interest.

Acknowledgements. The authors would like to thank Simon Pfreundschuh, currently at Chalmers University of Technology, for his guidance on the OEM functionality of ARTS. The authors would like to thank Lukas Kluft, currently at the Max Planck Institute for Meteorology in Hamburg, for his guidance on the calculation of heating rates with konrad and for helpful discussions along with Theresa Lang, currently

630

at Universität Hamburg (University of Hamburg). Finally, our thanks go to the ARTS radiative transfer community for their help with using ARTS.

635 *Financial support.* This work was funded by the German Research Foundation (DFG) in project ‘Elevated Moist Layers – Using HALO during EUREC4A to explore a blind spot in the global satellite observing system’, project BU 2253/9-1, part of DFG priority programme HALO SPP 1294, project number 316646266. It also is a contribution to the DFG-funded Cluster of Excellence “CLICCS—Climate, Climatic Change, and Society” (EXC 2037, Project Number 390683824), and to the Center for Earth System Research and Sustainability (CEN) of Universität Hamburg.

References

- 640 Albright, A. L., Fildier, B., Touzé-Peiffer, L., Pincus, R., Vial, J., and Muller, C.: Atmospheric radiative profiles during EUREC⁴A, Earth System Science Data, <https://doi.org/https://doi.org/10.5194/essd-2020-269>, 2020.
- Ananthakrishnan, R. and Kesavamurthy, R. N.: Some new features of the vertical distribution of temperature and humidity over Bombay, during the south-west monsoon season, *Journal of the Marine Biological Association of India*, 14, 732–742, <http://mbai.org.in/php/journaldownload.php?id=681&bkid=45>, 1972.
- 645 Anderson, G., Clough, S., Kneizys, F., Chetwynd, J., and Shettle, E.: AFGL Atmospheric Constituent Profiles (0.120km), p. 46, 1986.
- Berndt, E., Smith, N., Burks, J., White, K., Esmaili, R., Kuciauskas, A., Duran, E., Allen, R., LaFontaine, F., and Szkodzinski, J.: Gridded Satellite Sounding Retrievals in Operational Weather Forecasting: Product Description and Emerging Applications, *Remote Sensing*, 12, 3311, <https://doi.org/https://doi.org/10.3390/rs12203311>, 2020.
- Bony, S., Stevens, B., Frierson, D. M. W., Jakob, C., Kageyama, M., Pincus, R., Shepherd, T. G., Sherwood, S. C., Siebesma, A. P., Sobel, A. H., Watanabe, M., and Webb, M. J.: Clouds, circulation and climate sensitivity, *Nature Geoscience*, 8, 261–268, <https://doi.org/10.1038/ngeo2398>, 2015.
- 650 Borger, C., Schneider, M., Ertl, B., Hase, F., García, O. E., Sommer, M., Höpfner, M., Tjemkes, S. A., and Calbet, X.: Evaluation of MUSICA IASI tropospheric water vapour profiles using theoretical error assessments and comparisons to GRUAN Vaisala RS92 measurements, *Atmospheric Measurement Techniques*, 11, 4981–5006, <https://doi.org/https://doi.org/10.5194/amt-11-4981-2018>, 2018.
- 655 Boukachaba, N., Guidard, V., and Fourrié, N.: Land surface temperature retrieval from IASI for assimilation over the AROME-France domain, 2015.
- Buehler, S. A., Mendrok, J., Eriksson, P., Perrin, A., Larsson, R., and Lemke, O.: ARTS, the Atmospheric Radiative Transfer Simulator – version 2.2, the planetary toolbox edition, *Geoscientific Model Development*, 11, 1537–1556, <https://doi.org/https://doi.org/10.5194/gmd-11-1537-2018>, 2018.
- 660 Calbet, X., Schlüssel, P., Hultberg, T., Phillips, P., and August, T.: Validation of the operational IASI level 2 processor using AIRS and ECMWF data, *Advances in Space Research*, 37, 2299–2305, <https://doi.org/10.1016/j.asr.2005.07.057>, 2006.
- Cao, G., Giambelluca, T. W., Stevens, D. E., and Schroeder, T. A.: Inversion Variability in the Hawaiian Trade Wind Regime, *Journal of Climate*, 20, 1145–1160, <https://doi.org/10.1175/JCLI4033.1>, 2007.
- Chang, S., Sheng, Z., Du, H., Ge, W., and Zhang, W.: A channel selection method for hyperspectral atmospheric infrared sounders based on layering, *Atmospheric Measurement Techniques*, 13, 629–644, <https://doi.org/https://doi.org/10.5194/amt-13-629-2020>, 2020.
- 665 Chazette, P., Marnas, F., Totems, J., and Shang, X.: Comparison of IASI water vapor retrieval with H₂O-Raman lidar in the framework of the Mediterranean HyMeX and ChArMEx programs, *Atmospheric Chemistry and Physics*, 14, 9583–9596, <https://doi.org/10.5194/acp-14-9583-2014>, 2014.
- Clerbaux, C., Boynard, A., Clarisse, L., George, M., Hadji-Lazaro, J., Herbin, H., Hurtmans, D., Pommier, M., Razavi, A., Turquety, S., Wespes, C., and Coheur, P.-F.: Monitoring of atmospheric composition using the thermal infrared IASI/MetOp sounder, *Atmospheric Chemistry and Physics*, 9, 6041–6054, <https://doi.org/https://doi.org/10.5194/acp-9-6041-2009>, 2009.
- 670 Collard, A. D.: Selection of IASI channels for use in numerical weather prediction, *Quarterly Journal of the Royal Meteorological Society*, 133, 1977–1991, <https://doi.org/https://doi.org/10.1002/qj.178>, 2007.
- Coppens, D., Meyer, R., Klaes, D., and Montagner, F.: IASI Level 1: Product Guide, https://www-cdn.eumetsat.int/files/2020-04/pdf_iasi_pg.pdf, 2019.

- ECMWF: IFS Documentation - Cy45r1, chap. Part IV : Physical processes, p. 203, ECMWF, <https://www.ecmwf.int/node/18714>, 2018.
- Eresmaa, R. and McNally, A.: Diverse profile datasets from the ECMWF 137-level short-range forecasts, <https://doi.org/10.13140/2.1.4476.8963>, 2014.
- Eriksson, P., Buehler, S., Davis, C., Emde, C., and Lemke, O.: ARTS, the atmospheric radiative transfer simulator, version 2, *Journal of Quantitative Spectroscopy and Radiative Transfer*, 112, 1551–1558, <https://doi.org/10.1016/j.jqsrt.2011.03.001>, 2011.
- EUMETSAT: IASI Level 2: Product Guide, 2017.
- Fourrié, N. and Rabier, F.: Cloud characteristics and channel selection for IASI radiances in meteorologically sensitive areas, *Quarterly Journal of the Royal Meteorological Society*, 130, 1839–1856, <https://doi.org/https://doi.org/10.1256/qj.03.27>, 2004.
- Fourrié, N. and Thépaut, J.-N.: Evaluation of the AIRS near-real-time channel selection for application to numerical weather prediction, *Quarterly Journal of the Royal Meteorological Society*, 129, 2425–2439, <https://doi.org/https://doi.org/10.1256/qj.02.210>, 2003.
- Gordon, I., Rothman, L., Hill, C., Kochanov, R., Tan, Y., Bernath, P., Birk, M., Boudon, V., Campargue, A., Chance, K., Drouin, B., Flaud, J.-M., Gamache, R., Hodges, J., Jacquemart, D., Perevalov, V., Perrin, A., Shine, K., Smith, M.-A., Tennyson, J., Toon, G., Tran, H., Tyuterev, V., Barbe, A., Császár, A., Devi, V., Furtenbacher, T., Harrison, J., Hartmann, J.-M., Jolly, A., Johnson, T., Karman, T., Kleiner, I., Kyuberis, A., Loos, J., Lyulin, O., Massie, S., Mikhailenko, S., Moazzen-Ahmadi, N., Müller, H., Naumenko, O., Nikitin, A., Polyansky, O., Rey, M., Rotger, M., Sharpe, S., Sung, K., Starikova, E., Tashkun, S., Auwera, J. V., Wagner, G., Wilzewski, J., Wcisło, P., Yu, S., and Zak, E.: The HITRAN2016 molecular spectroscopic database, *Journal of Quantitative Spectroscopy and Radiative Transfer*, 203, 3–69, <https://doi.org/https://doi.org/10.1016/j.jqsrt.2017.06.038>, 2017.
- Haraguchi, P. Y.: Inversions over the tropical eastern pacific ocean, *Monthly Weather Review*, 96, 177 – 185, [https://doi.org/10.1175/1520-0493\(1968\)096<0177:IOTTEP>2.0.CO;2](https://doi.org/10.1175/1520-0493(1968)096<0177:IOTTEP>2.0.CO;2), https://journals.ametsoc.org/view/journals/mwre/96/3/1520-0493_1968_096_0177_iottep_2_0_co_2.xml, 1968.
- Irion, F. W., Kahn, B. H., Schreier, M. M., Fetzner, E. J., Fishbein, E., Fu, D., Kalmus, P., Wilson, R. C., Wong, S., and Yue, Q.: Single-footprint retrievals of temperature, water vapor and cloud properties from AIRS, *Atmospheric Measurement Techniques*, 11, 971–995, <https://doi.org/https://doi.org/10.5194/amt-11-971-2018>, 2018.
- Johnson, R. H., Ciesielski, P. E., and Hart, K. A.: Tropical Inversions near the 0°C Level, *Journal of the Atmospheric Sciences*, 53, 1838–1855, [https://doi.org/10.1175/1520-0469\(1996\)053<1838:TINTL>2.0.CO;2](https://doi.org/10.1175/1520-0469(1996)053<1838:TINTL>2.0.CO;2), 1996.
- Johnson, R. H., Rickenbach, T. M., Rutledge, S. A., Ciesielski, P. E., and Schubert, W. H.: Trimodal Characteristics of Tropical Convection, *Journal of Climate*, 12, 2397–2418, [https://doi.org/10.1175/1520-0442\(1999\)012<2397:TCOTC>2.0.CO;2](https://doi.org/10.1175/1520-0442(1999)012<2397:TCOTC>2.0.CO;2), [https://doi.org/10.1175/1520-0442\(1999\)012<2397:TCOTC>2.0.CO;2](https://doi.org/10.1175/1520-0442(1999)012<2397:TCOTC>2.0.CO;2), 1999.
- Kluft, L. and Dacie, S.: `atmtools/konrad`: Add line-by-line radiation and conceptual clouds, <https://doi.org/http://doi.org/10.5281/zenodo.3899702>, 2020.
- Konow, H., Jacob, M., Ament, F., Crewell, S., Ewald, F., Hagen, M., Hirsch, L., Jansen, F., Mech, M., and Stevens, B.: A unified data set of airborne cloud remote sensing using the HALO Microwave Package (HAMP), *Earth System Science Data*, 11, 921–934, <https://doi.org/https://doi.org/10.5194/essd-11-921-2019>, 2019.
- Lacour, J.-L., Risi, C., Clarisse, L., Bony, S., Hurtmans, D., Clerbaux, C., and Coheur, P.-F.: Mid-tropospheric D observations from IASI/MetOp at high spatial and temporal resolution, *Atmospheric Chemistry and Physics*, 12, 10 817–10 832, <https://doi.org/10.5194/acp-12-10817-2012>, 2012.
- Lerner, J. A.: Temperature and humidity retrieval from simulated Infrared Atmospheric Sounding Interferometer (IASI) measurements, *Journal of Geophysical Research*, 107, <https://doi.org/10.1029/2001JD900254>, 2002.

- Levenberg, K.: A method for the solution of certain non-linear problems in least squares, *Quarterly of Applied Mathematics*, 2, 164–168, <https://doi.org/10.1090/qam/10666>, 1944.
- 715
- Marquardt, D. W.: An Algorithm for Least-Squares Estimation of Nonlinear Parameters, *Journal of the Society for Industrial and Applied Mathematics*, 11, 431–441, <https://doi.org/10.1137/0111030>, 1963.
- Martinet, P., Lavanant, L., Fourrié, N., Rabier, F., and Gambacorta, A.: Evaluation of a revised IASI channel selection for cloudy retrievals with a focus on the Mediterranean basin, *Quarterly Journal of the Royal Meteorological Society*, 140, 1563–1577, <https://doi.org/https://doi.org/10.1002/qj.2239>, 2013.
- 720
- Matricardi, M., López-Puertas, M., and Funke, B.: Modeling of Nonlocal Thermodynamic Equilibrium Effects in the Classical and Principal Component-Based Version of the RTTOV Fast Radiative Transfer Model, *Journal of Geophysical Research: Atmospheres*, 123, 5741–5761, <https://doi.org/https://doi.org/10.1029/2018JD028657>, 2018.
- Mauritsen, T. and Stevens, B.: Missing iris effect as a possible cause of muted hydrological change and high climate sensitivity in models, *Nature Geoscience*, 8, 346–351, <https://doi.org/10.1038/NNGEO2414>, 2015.
- 725
- Merchant, C. J., Embury, O., Bulgin, C. E., Block, T., Corlett, G. K., Fiedler, E., Good, S. A., Mittaz, J., Rayner, N. A., Berry, D., Eastwood, S., Taylor, M., Tsushima, Y., Waterfall, A., Wilson, R., and Donlon, C.: Satellite-based time-series of sea-surface temperature since 1981 for climate applications, *Scientific Data*, 6, <https://doi.org/https://doi.org/10.1038/s41597-019-0236-x>, 2019.
- Mlawer, E. J., Taubman, S. J., Brown, P. D., Iacono, M. J., and Clough, S. A.: Radiative transfer for inhomogeneous atmospheres: RRTM, a validated correlated-k model for the longwave, *Journal of Geophysical Research: Atmospheres*, 102, 16 663–16 682, <https://doi.org/https://doi.org/10.1029/97JD00237>, 1997.
- 730
- Mlawer, E. J., Payne, V. H., Moncet, J.-L., Delamere, J. S., Alvarado, M. J., and Tobin, D. C.: Development and recent evaluation of the MT_CKD model of continuum absorption, *Philosophical Transactions of the Royal Society A: Mathematical, Physical and Engineering Sciences*, 370, 2520–2556, <https://doi.org/https://doi.org/10.1098/rsta.2011.0295>, 2012.
- 735
- Muller, C. and Bony, S.: What favors convective aggregation and why?, *Geophysical Research Letters*, 42, 5626–5634, <https://doi.org/10.1002/2015GL064260>, 2015.
- Posselt, D. J., van den Heever, S. C., and Stephens, G. L.: Trimodal cloudiness and tropical stable layers in simulations of radiative convective equilibrium, *Geophysical Research Letters*, 35, <https://doi.org/https://doi.org/10.1029/2007GL033029>, 2008.
- 740
- Prange, M., Brath, M., and Buehler, S. A.: Supplementary data for "Are elevated moist layers a blind spot for hyperspectral infrared sounders? - a model study", <https://doi.org/10.5281/zenodo.4501184>, 2021.
- Razavi, A., Clerbaux, C., Wespes, C., Clarisse, L., Hurtmans, D., Payan, S., Camy-Peyret, C., and Coheur, P. F.: Characterization of methane retrievals from the IASI space-borne sounder, *Atmospheric Chemistry and Physics*, 9, 7889–7899, <https://doi.org/https://doi.org/10.5194/acp-9-7889-2009>, 2009.
- Rodgers, C. D.: *Inverse Methods for Atmospheric Sounding*, <https://doi.org/https://doi.org/10.1142/3171>, 2000.
- 745
- Romps, D. M.: An Analytical Model for Tropical Relative Humidity, *Journal of Climate*, 27, 7432–7449, <https://doi.org/https://doi.org/10.1175/JCLI-D-14-00255.1>, 2014.
- Schneider, M. and Hase, F.: Optimal estimation of tropospheric H₂O and δD with IASI/METOP, *Atmospheric Chemistry and Physics*, 11, 11 207–11 220, <https://doi.org/10.5194/acp-11-11207-2011>, 2011.
- Smith, N. and Barnett, C. D.: Uncertainty Characterization and Propagation in the Community Long-Term Infrared Microwave Combined Atmospheric Product System (CLIMCAPS), *Remote Sensing*, 11, 1227, <https://doi.org/https://doi.org/10.3390/rs11101227>, 2019.
- 750

- Smith, N. and Barnett, C. D.: CLIMCAPS observing capability for temperature, moisture, and trace gases from AIRS/AMSU and CrIS/ATMS, *Atmospheric Measurement Techniques*, 13, 4437–4459, <https://doi.org/https://doi.org/10.5194/amt-13-4437-2020>, 2020.
- Smith, W. and Weisz, E.: Dual-Regression Approach for High-Spatial-Resolution Infrared Soundings, pp. 297–311, <https://doi.org/https://doi.org/10.1016/B978-0-12-409548-9.10394-X>, 2018.
- 755 Smith, W. L., Weisz, E., Kireev, S. V., Zhou, D. K., Li, Z., and Borbas, E. E.: Dual-Regression Retrieval Algorithm for Real-Time Processing of Satellite Ultraspectral Radiances, *Journal of Applied Meteorology and Climatology*, 51, 1455–1476, <https://doi.org/10.1175/JAMC-D-11-0173.1>, 2012.
- Sobel, A. H. and Bretherton, C. S.: Modeling Tropical Precipitation in a Single Column, *Journal of Climate*, 13, 4378–4392, [https://doi.org/10.1175/1520-0442\(2000\)013<4378:MTPIAS>2.0.CO;2](https://doi.org/10.1175/1520-0442(2000)013<4378:MTPIAS>2.0.CO;2), [https://doi.org/10.1175/1520-0442\(2000\)013<4378:MTPIAS>2.0.CO;2](https://doi.org/10.1175/1520-0442(2000)013<4378:MTPIAS>2.0.CO;2), 2000.
- 760 Stevens, B., Brogniez, H., Kiemle, C., Lacour, J.-L., Crevoisier, C., and Kiliani, J.: Structure and Dynamical Influence of Water Vapor in the Lower Tropical Troposphere, *Surveys in Geophysics*, 38, 1371–1397, <https://doi.org/https://doi.org/10.1007/s10712-017-9420-8>, 2017.
- Stevens, B., Bony, S., Farrell, D., Ament, F., Blyth, A., Fairall, C., Karstensen, J., Quinn, P. K., Speich, S., Acquistapace, C., Aemisegger, F., Albright, A. L., Bellenger, H., Bodenschatz, E., Caesar, K.-A., Chewitt-Lucas, R., de Boer, G., Delanoë, J., Denby, L., Ewald, F., Fildier, B., Forde, M., George, G., Gross, S., Hagen, M., Hausold, A., Heywood, K. J., Hirsch, L., Jacob, M., Jansen, F., Kinne, S., Klocke, D., Kölling, T., Konow, H., Lathon, M., Mohr, W., Naumann, A. K., Nuijens, L., Olivier, L., Pincus, R., Pöhlker, M., Reverdin, G., Roberts, G., Schnitt, S., Schulz, H., Siebesma, A. P., Stephan, C. C., Sullivan, P., Touzé-Peiffer, L., Vial, J., Vogel, R., Zuidema, P., Alexander, N., Alves, L., Arixi, S., Asmath, H., Bagheri, G., Baier, K., Bailey, A., Baranowski, D., Baron, A., Barrau, S., Barrett, P. A., Batier, F., Behrendt, A., Bendinger, A., Beucher, F., Bigorre, S., Blades, E., Blossey, P., Bock, O., Böing, S., Bossler, P., Bourras, D., Bouruet-Aubertot, P., Bower, K., Branellec, P., Branger, H., Brennek, M., Brewer, A., Brilouet, P.-E., Brüggemann, B., Buehler, S. A., Burke, E., Burton, R., Calmer, R., Canonici, J.-C., Carton, X., Cato Jr., G., Charles, J. A., Chazette, P., Chen, Y., Chilinski, M. T., Choulaton, T., Chuang, P., Clarke, S., Coe, H., Cornet, C., Coutris, P., Couvreux, F., Crewell, S., Cronin, T., Cui, Z., Cuypers, Y., Daley, A., Damerell, G. M., Dauhut, T., Deneke, H., Desbios, J.-P., Dörner, S., Donner, S., Douet, V., Drushka, K., Dütsch, M., Ehrlich, A., Emanuel, K., Emmanouilidis, A., Etienne, J.-C., Etienne-Leblanc, S., Faure, G., Feingold, G., Ferrero, L., Fix, A., Flamant, C., Flatau, P. J., Foltz, G. R., Forster, L., Furtuna, I., Gadian, A., Galewsky, J., Gallagher, M., Gallimore, P., Gaston, C., Gentemann, C., Geyskens, N., Giez, A., Gollop, J., Gouirand, I., Goubeyre, C., de Graaf, D., de Groot, G. E., Grosz, R., Güttler, J., Gutleben, M., Hall, K., Harris, G., Helfer, K. C., Henze, D., Herbert, C., Holanda, B., Ibanez-Landeta, A., Intrieri, J., Iyer, S., Julien, F., Kalesse, H., Kazil, J., Kellman, A., Kidane, A. T., Kirchner, U., Klingebiel, M., Körner, M., Kremper, L. A., Kretzschmar, J., Krüger, O., Kumala, W., Kurz, A., L'Hégaret, P., Labaste, M., Lachlan-Cope, T., Laing, A., Landschützer, P., Lang, T., Lange, D., Lange, I., Laplace, C., Lavik, G., Laxenaire, R., Le Bihan, C., Leandro, M., Lefevre, N., Lena, M., Lenschow, D., Li, Q., Lloyd, G., Los, S., Losi, N., Lovell, O., Luneau, C., Makuch, P., Malinowski, S., Manta, G., Marinou, E., Marsden, N., Masson, S., Maury, N., Mayer, B., Mayers-Als, M., Mazel, C., McGeary, W., McWilliams, J. C., Mech, M., Mehlmann, M., Meroni, A. N., Mieslinger, T., Minikin, A., Minnett, P., Möller, G., Morfa Avalos, Y., Muller, C., Musat, I., Napoli, A., Neuberger, A., Noisel, C., Noone, D., Nordsiek, F., Nowak, J. L., Oswald, L., Parker, D. J., Peck, C., Person, R., Philippi, M., Plueddemann, A., Pöhlker, C., Pörtge, V., Pöschl, U., Pologne, L., Posniak, M., Prange, M., Quiñones Meléndez, E., Radtke, J., Ramage, K., Reimann, J., Renault, L., Reus, K., Reyes, A., Ribbe, J., Ringel, M., Ritschel, M., Rocha, C. B., Rochetin, N., Röttenbacher, J., Rollo, C., Royer, H., Sadoulet, P., Saffin, L., Sandiford, S., Sandu, I., Schäfer, M., Schemann, V., Schirmacher, I., Schlenczek, O., Schmidt, J., Schröder, M., Schwarzenboeck, A., Sealy, A., Senff, C. J., Serikov, I., Shohan, S., Siddle, E., Smirnov, A., Späth, F., Spooner, B., Stolla, M. K., Szkółka, W., de Szoeko, S. P., Tarot, S., Tetoni, E., Thompson, E., Thomson, J., Tomassini, L., Totems, J., Ubele, A. A., Villiger, L.,

- 790 von Arx, J., Wagner, T., Walther, A., Webber, B., Wendisch, M., Whitehall, S., Wiltshire, A., Wing, A. A., Wirth, M., Wiskandt, J., Wolf, K., Worbes, L., Wright, E., Wulfmeyer, V., Young, S., Zhang, C., Zhang, D., Ziemer, F., Zinner, T., and Zöger, M.: EUREC⁴A, Earth System Science Data Discussions, 2021, 1–78, <https://doi.org/10.5194/essd-2021-18>, <https://essd.copernicus.org/preprints/essd-2021-18/>, 2021.
- 795 Susskind, J., Blaisdell, J. M., and Iredell, L.: Improved methodology for surface and atmospheric soundings, error estimates, and quality control procedures: the atmospheric infrared sounder science team version-6 retrieval algorithm, *Journal of Applied Remote Sensing*, 8, 084994, <https://doi.org/https://doi.org/10.1117/1.JRS.8.084994>, 2014.
- Weisz, E., Smith, W. L., and Smith, N.: Advances in simultaneous atmospheric profile and cloud parameter regression based retrieval from high-spectral resolution radiance measurements, *Journal of Geophysical Research: Atmospheres*, 118, 6433–6443, <https://doi.org/10.1002/jgrd.50521>, 2013.
- 800 Zhou, D. K., Smith, W. L., Larar, A. M., Liu, X., Taylor, J. P., Schlüssel, P., Strow, L. L., and Mango, S. A.: All weather IASI single field-of-view retrievals: case study – validation with JAIVEx data, *Atmospheric Chemistry and Physics*, 9, 2241–2255, <https://doi.org/https://doi.org/10.5194/acp-9-2241-2009>, 2009.
- Zuidema, P.: The 600–800-mb Minimum in Tropical Cloudiness Observed during TOGA COARE, *Journal of the Atmospheric Sciences*, 55, 2220–2228, [https://doi.org/10.1175/1520-0469\(1998\)055<2220:TMMITC>2.0.CO;2](https://doi.org/10.1175/1520-0469(1998)055<2220:TMMITC>2.0.CO;2), [https://doi.org/10.1175/1520-0469\(1998\)055<2220:TMMITC>2.0.CO;2](https://doi.org/10.1175/1520-0469(1998)055<2220:TMMITC>2.0.CO;2), 1998.